International Journal of Earth Sciences

Karst bauxite formation during Miocene Climatic Optimum (central Dalmatia, Croatia): mineralogical, compositional and geochronological perspectives

--Manuscript Draft--

Manuscript Number:	
Full Title:	Karst bauxite formation during Miocene Climatic Optimum (central Dalmatia, Croatia): mineralogical, compositional and geochronological perspectives
Article Type:	Original Paper
Keywords:	karst bauxite, CA-ID-TIMS zircon geochronology, maximum depositional age, kaolinite and gibbsite, Miocene Climatic Optimum, central Dalmatia
Corresponding Author:	Mihovil Brlek, Ph.D. Croatian Geological Survey Zagreb, CROATIA
Corresponding Author Secondary Information:	
Corresponding Author's Institution:	Croatian Geological Survey
Corresponding Author's Secondary Institution:	
First Author:	Mihovil Brlek, Ph.D.
First Author Secondary Information:	
Order of Authors:	Mihovil Brlek, Ph.D.
	Sean P Gaynor, Ph.D.
	Giovanni Mongelli, Ph.D.
	Blanca Bauluz, Ph.D.
	Rosa Sinisi, Ph.D.
	Vlatko Brčić, Ph.D.
	Irena Peytcheva, Ph.D.
	Ivan Mišur, Ph.D.
	Simon Richard Tapster, Ph.D.
	Nina Trinajstić, MSc
	Elisa Laita, Ph.D.
	Alfonso Yuste, Ph.D.
	Sanja Šuica, Ph.D.
	Anita Grizelj, Ph.D.
	Duje Kukoč, Ph.D.
	Urs Schaltegger, Ph.D.
Order of Authors Secondary Information:	
Funding Information:	Hrvatska Zaklada za Znanost (HRZZ UIP-2019-04-7761) Dr. Mihovil Brlek
Abstract:	The Miocene Climatic Optimum (MCO) represents a global warm period (approximately 17–14.7 Ma) interrupting a long-term period of Cenozoic cooling. In order to elucidate if bauxitization took place in southeastern European mid-latitude areas during the MCO, we studied a section of undated massive karst bauxite (Crveni Klanac, CK) in central Dalmatia, Croatia, hosted in Upper Cretaceous limestones and

	overlain by Miocene Sinj Basin lacustrine deposits. Integrated mineralogical, morphological and geochemical analyses indicate the predominant mineral phases of the homogenous bauxite matrix are authigenic, subhedral to euhedral kaolinite and gibbsite. The in situ mineralization was a consequence of edaphic processes under prevailing alkaline pH conditions, indicating the CK bauxites formed in autochthonous conditions. In situ U-Pb zircon ages of the lower, middle and upper parts of the CK bauxite are very similar, dominated by Miocene and Oligocene ages, indicating they all share similar protolith(s). Subsequent high-precision chemical abrasion-isotope dilution-thermal ionization mass spectrometry (CA-ID-TIMS) analyses indicate a maximum depositional age (MDA) for bauxite parent material of 16.9576 ± 0.0096/0.011/0.021 Ma. This MDA, a maximum age of autochthonous bauxitization, coincides with the onset of the MCO. Based on currently available geochronological constraints, the maximum timeframe for CK bauxitization was less than ~700 ka, which matches the records of the MCO in paleo-mid-latitude Europe. More than simply aligning with regional and local reconstructions of continental climatic conditions during the onset and the early stages of the MCO, the CK autochtonous bauxites provide a precise climatic constraint. In order for in-situ bauxitization to occur in southeastern parts of the mid-latitude continental European areas, paleoclimatic and paleoenvironmental conditions must have had mean annual temperature greater than 17–22°C and mean annual precipitation of more than 1100–1200 mm.

Karst bauxite formation during Miocene Climatic Optimum (central Dalmatia, Croatia): mineralogical, compositional and geochronological perspectives

Mihovil Brlek[1], Sean P. Gaynor[2], Giovanni Mongelli[3], Blanca Bauluz[4], Rosa Sinisi[3], Vlatko Brčić[1], Irena Peytcheva[5], Ivan Mišur[1], Simon Tapster[6], Nina Trinajstić[1], Elisa Laita[4], Alfonso Yuste[4], Sanja Šuica[7], Anita Grizelj[1], Duje Kukoč[1], Urs Schaltegger[2]

[1]Croatian Geological Survey, Department of Geology, Sachsova 2, HR-10000 Zagreb, Croatia

[2]University of Geneva, Department of Earth Sciences, Rue des Maraichers 13, 1205-CH Geneva, Switzerland

[3]University of Basilicata, Department of Sciences, Viale Ateneo Lucano 10, Potenza 85100, Italy

[4]Universidad de Zaragoza, IUCA-Departamento de Ciencias de la Tierra, Pedro Cerbuna 12, 50009 Zaragoza, Spain

[5]Bulgarian Academy of Sciences, Geological Institute, Acad. G. Bonchev Bl. 24, 1113 Sofia, Bulgaria

[6]British Geological Survey, NERC Isotope Geosciences Facilities, Nicker Hill, Keyworth, Nottingham, NG12 5GG United Kingdom

[7]INA-Industrija nafte, d.d., Rock and Fluid Analysis, Lovinčićeva 4, HR-10000 Zagreb, Croatia

Corresponding author. E-mail: mihovil.brlek@hgi-cgs.hr

Abstract

The Miocene Climatic Optimum (MCO) represents a global warm period (approximately 17–14.7 Ma) interrupting a long-term period of Cenozoic cooling. In order to elucidate if bauxitization took place in southeastern European mid-latitude areas during the MCO, we studied a section of undated massive karst bauxite (Crveni Klanac, CK) in central Dalmatia, Croatia, hosted in Upper Cretaceous limestones and overlain by Miocene Sinj Basin lacustrine deposits. Integrated mineralogical, morphological and geochemical analyses indicate the predominant mineral phases of the homogenous bauxite matrix are authigenic, subhedral to euhedral kaolinite and gibbsite. The *in situ* mineralization was a consequence of edaphic processes under prevailing alkaline pH conditions, indicating the CK bauxites formed in autochthonous conditions. *In situ* U-Pb zircon ages of the lower, middle and upper parts of the CK bauxite are very similar, dominated by Miocene and Oligocene ages, indicating they all share similar protolith(s). Subsequent high-precision chemical abrasion-isotope dilution-thermal ionization mass spectrometry

(CA-ID-TIMS) analyses indicate a maximum depositional age (MDA) for bauxite parent material of 16.9576 ± 0.0096/0.011/0.021 Ma. This MDA, a maximum age of autochthonous bauxitization, coincides with the onset of the MCO. Based on currently available geochronological constraints, the maximum timeframe for CK bauxitization was less than ~700 ka, which matches the records of the MCO in paleo-mid-latitude Europe. More than simply aligning with regional and local reconstructions of continental climatic conditions during the onset and the early stages of the MCO, the CK autochtonous bauxites provide a precise climatic constraint. In order for *in-situ* bauxitization to occur in southeastern parts of the mid-latitude continental European areas, paleoclimatic and paleoenvironmental conditions must have had mean annual temperature greater than 17–22°C and mean annual precipitation of more than 1100–1200 mm.

Keywords: karst bauxite, CA-ID-TIMS zircon geochronology, maximum depositional age, kaolinite and gibbsite, Miocene Climatic Optimum, central Dalmatia

Declarations

Funding

The work has been supported in part by Croatian Science Foundation under the project "Miocene syn-rift evolution of the North Croatian Basin (Carpathian-Pannonian Region): a multi-proxy approach, correlation and integration of sedimentary and volcanic record" (PYROSKA, HRZZ UIP-2019-04-7761)

Conflicts of interest/Competing interests

The authors declare no Conflicts of interest/Competing interests

Availability of data and material

All data generated or analyzed during this study are included in this article (and its supplementary information files)

Code availability

Not applicable

Author's contributions

All authors contributed to the study conception and design. Material preparation, data collection and analysis were performed by Mihovil Brlek, Sean Gaynor, Giovanni Mongelli, Blanca Bauluz, Rosa Sinisi, Vlatko Brčić, Irena Peytcheva, Ivan Mišur, Simon Tapster, Nina Trinajstić, Elisa Laita, Alfonso Yuste, Sanja Šuica, Anita Grizelj, Duje Kukoč, and Urs Schaltegger. The first draft of the manuscript was written by Mihovil Brlek and Sean Gaynor and all authors commented on versions of the manuscript. All authors read and approved the final manuscript.

Acknowledgments

This work was partly supported by the Croatian Science Foundation under the project "Miocene syn-rift evolution of the North Croatian Basin (Carpathian–Pannonian Region): a multi-proxy approach, correlation and integration of sedimentary and volcanic record" (PYROSKA, HRZZ UIP-2019-04-7761). The research was also funded by the Spanish government (RTI2018-093419-B-I00). Authors would like to acknowledge the use of Servicio General de Apoyo a la Investigación-SAI, Universidad de Zaragoza. We dedicate this work to Ante Šušnjara and Biserka Šćavničar. We would like to thank Nikolina Ilijanić and Department of Mineral Resources of the Croatian Geological Survey for providing us the required legacy maps and data. We also thank Alan Vranjković for field assistance and discussions concerning the Sinj Basin evolution.

Introduction

Continental paleoclimate records are essential for reconstructions of past climate changes, better understanding modern climate and potential for future climate change (Bárdossy and Combes 1999; Retallack 2010; Retallack et al. 2016 and references therein; Methner et al. 2020). Bauxites are residual deposits which form due to intense chemical weathering in hot and humid zones (generally in humid tropical and sub-tropical climates) and are enriched in Al by removing other cations (e.g., Si, alkali metal and REE; Bárdossy and Combes 1999; Bogatyrev et al. 2009; Retallack 2010; Huang et al. 2012; Mindszenty 2016), and therefore these deposits can serve as direct terrestrial paleoclimate indicators, particularly where their temporal record of formation can be well constrained. They are composed of Al hydroxides, with subordinate phyllosilicates (mainly kaolinite), Fe oxides and hydroxides, Ti oxides and a variety of other minerals. The chemical processes involved in formation of karst bauxites, confined to karst zones of carbonate rocks (e.g., Bárdossy 1982; Bárdossy and Combes 1999; Mondillo et al. 2011; Mongelli et al. 2014; Yuste et al. 2015), is almost the same as that for lateritic bauxites, formed as result of a strong chemical weathering of aluminosilicate rocks (e.g., Eggleton et al. 2008; Singh et al. 2018). However, karst bauxites may gain Al from a variety of sources (see also Liu et al. 2013; Liu et al. 2019 and references therein). These include volcaniclastic deposits, as well as resedimented pre-existing bauxite deposits (Comer 1974; Bogatyrev et al. 2009; Kelemen et al. 2017). Bauxites are unevenly distributed through time, with unusually widespread and intense formation of bauxite (and laterite) associated with distinct temporal peaks identified at 2, 12, 16, 35, 48, 55, 65 and 100 Ma (Retallack 2010). During these peaks, bauxites and laterites are found at unusually high latitudes, and these periods are coeval with CO_2 greenhouse events, times of global high warmth and precipitation, elevated atmospheric carbon dioxide and oceanic anoxia (Bárdossy and Combes 1999; Retallack 2010; Mindszenty 2016). The Miocene Climatic Optimum (MCO; ca. 17–15 Ma) was a CO_2 greenhouse event associated with a global warm and humid climate (Kasbohm and Schoene 2018; Methner et al. 2020 and references therein; Sosdian et al. 2020), and these conditions may have allowed for lateritization and bauxitization to potentially extended mid-latitude areas, beyond the tropical modern extent of laterites and bauxites (Retallack 2010). Lateritic bauxites associated with the MCO have previously been identified with the Columbia River Basalts (CRB) in Oregon and Washington in the United States (Liu et al. 2013; Retallack et al. 2016; Kasbohm and Schoene 2018), as well as with intense chemical weathering of Vogelsberg basalts in central Germany (Schwarz 1997).

Central Dalmatian karst bauxites in the Sinj area (Croatia) are found in several stratigraphic horizons (Šušnjara et al. 1990), including massive clayey bauxites hosted predominantly in Upper Cretaceous carbonate platform limestones and underlying the Miocene transgressive Dinaride Lake System Basin deposits (DLSB; Sinj Basin – SB; Šušnjara and Sakač 1988; de Leeuw et al. 2010). Their genesis has been interpreted to reflect Oligocene–Miocene *in situ* bauxitization of mixed detritus, including volcaniclastic material (Šušnjara and Šćavničar 1976, 1978; Šušnjara et al. 1990). These interpretations were based on the presence and abundance of euhedral, prismatic zircon grains found in the heavy mineral assemblage of these bauxites, which are absent from older regional bauxites, but present in Miocene SB volcaniclastic deposits.

In order to define the genesis and age of Central Dalmatian karst bauxites underlying DLSB deposits, we present a multi-proxy approach applied on bauxites from the Crveni Klanac (CK) section. In order to resolve if the CK bauxites were formed *in situ* (autochthonous), or were deposited as the result of recycling of older bauxite horizons, we integrated mineralogical, textural, morphological and geochemical analyses of several bauxite horizons (e.g., Huang et al. 2012; Mongelli et al. 2014; Yuste et al. 2015, 2020; Kelemen et al. 2017, 2020; Singh et al. 2018; Sinisi 2018). These data also yield significant interpretations about the parental affinity and post-genetic modifications for the CK bauxites. In addition, we use detrital zircon U-Pb geochronology to generate the maximum depositional age (MDA) of the bauxite parental material based on the law of detrital zircon: a sedimentary rock cannot be older than the youngest zircon crystal it contains (Gehrels 2014; Herriot et al. 2019; Sharman and Malkowski 2020). We utilize laser ablation-inductively coupled plasma-mass spectrometry (LA-ICP-MS) U-Pb analyses to screen the ages of the detrital zircon (e.g., Liu et al. 2014; Kelemen et al. 2017). However, LA-ICP-MS geochronology is relatively limited in precision and accuracy, and therefore the youngest identified population of zircon grains was extracted for further analysis using high-precision chemical abrasion-isotope dilution-thermal ionization mass spectrometry (CA-ID-TIMS) (Gehrels 2014; Schaltegger et al. 2015; Herriott et al. 2019; Sharman and Malkowski 2020). The U-Pb age spectra from these detrital zircon enables preliminary insight into potential regional (e.g., Carpathian-Pannonian Region - CPR - volcanism; Lukács et al. 2018; Brlek et al. 2020) and local magmatic sources that could have provided detrital material to the CK bauxite. Lower–Middle Miocene volcaniclastic rocks, interlaid in lacustrine deposits within the SB and other surrounding intra-montane basins (Šušnjara and Šćavničar 1974), were previously used to construct chronologic framework for the DLSB sediments (de Leeuw et al. 2010; de Leeuw et al. 2012 and references therein). A new high-precision U-Pb zircon date of the oldest volcaniclastic horizon within the SB further refines the depositional history of the basin, and subsequently helps elucidate how bauxite formation may have occurred on a regional scale. This updated model for the geologic history of this region helps to elucidate the weathering processes affected by paleoclimate and prevailing paleoenvironmental conditions during formation of bauxite mineral associations. Our new high-precision zircon geochronological constraints, supported with CK bauxite compositional data, imply that the bauxitization in mid-latitude European terrestrial areas occurred during the MCO global warm climate, leaving a physical record of the interruption of long-term Cenozoic cooling.

Geological and stratigraphic framework of Miocene karst bauxites (central Dalmatia, Croatia)

The Sinj Basin (SB) is a NW-SE striking elongated basin located in southeastern Croatia (central Dalmatia) on the SE margin of the External Dinarides, and interpreted to have formed as a pull-apart structure (Fig. 1a, b; Mandic et al. 2008). It is one of numerous, synchronous parallel basins (Fig. 1a) which formed within the Western Thrust Belt of the Dinarides during the Early Miocene as a result of either transpressional tectonics (Mandic et al. 2008), or extension (de Leeuw et al. 2012; van Unen et al. 2019 and references therein; Mandic et al. 2020). These intra-montane basins host MCO-related lacustrine deposits referred to as the DLSB deposits (de Leeuw et al. 2012 and references therein; Mandic et al. 2020). The Dinaridic Western Thrust Belt is composed of Mesozoic to early Cenozoic Adriatic–Dinaridic Carbonate Platform deposits (Tari-Kovačić 1994; Mandic et al. 2008). With the onset of compressional tectonics during the Eocene, the platform turned into a foredeep, hosting flysch and molasse deposits (Promina Formation; Korbar 2009; Zupanič and Babić 2011), and was subsequently subaerially exposed during the Oligocene. The basin is surrounded by Triassic to Eocene carbonate rocks (also Eocene-Oligocene deposits in its western part), and has been deformed in the western part by the doming of Permo-Triassic evaporites (Fig. 1b; Mandic et al. 2008).

The Early to Middle Miocene SB lacustrine succession (palaeobiogeographically part of the DLSB) has an average thickness of 370 m and is divided into 3 main lithological units (Fig. 1b, c; Šušnjara and Šćavničar 1974; Šušnjara and Sakač 1988). The lower unit comprises variously colored marls in the northwestern and coal-bearing beds and marls with dreissenid bivalves in the southeastern part of the basin (Fig. 1b, c; Šušnjara and Sakač 1988; Mandic et al. 2008; de Leeuw et al. 2010). Although the two types of deposits of the basal unit were interpreted as being synchronous, lateral transitions or contacts between the two have not been recorded in the field (Šušnjara and Sakač 1988). The base of the lower unit, and therefore the onset of the lacustrine sedimentation in the SB, has been previously dated via Ar/Ar (biotite) of the Lučane-3 (LUČ-3) volcanoclastic horizon as 17.91±0.18 Ma (de Leeuw et al. 2010, 2012). However, this volcaniclastic horizon only occurs intercalated with variously colored marls in the northwestern part of the basin (Fig. 1b, c), and therefore only constrains the age of this type of deposit of the lower SB unit. The Lučane-2 (LUČ-2) volcaniclastic horizon, which occurs intercalated with clay-rich limestone's and limy marls in the northwestern part of the middle SB unit (with the middle unit lying concordantly on both lithological types of the lower unit), has been dated as deposited at 16.24±0.16 Ma, based on Ar/Ar sanidine geochronology (Fig. 1c; de Leeuw et al. 2010, 2012).

Bauxites hosted in karstified Upper Cretaceous carbonate platform limestones and Paleogene deposits can be found at the southwestern margin (Trilj area; e.g., Crveni Klanac – CK – section) and northern part of the SB (Fig. 1b, c; Šušnjara and Sakač 1988; Šušnjara et al. 1990). They are overlain by Miocene SB lacustrine deposits of coal-bearing beds and marls with dreissenid bivalves of the lower SB unit (southwestern margin of the SB) and limestones and marls of middle SB unit (where the lower unit is absent; northern part of the SB). Massive bauxites, ranging from clayey bauxites to bauxitic clay horizons accumulated in pre-Miocene karstified paleo-depressions, which developed due to tectonics, erosion and weathering from the Oligocene to Early Miocene, and formed ore bodies which are defined as irregular, elongated lenses (Šušnjara et al. 1990; Mandic et al. 2008). The formation of the karstic network in Upper Cretaceous rocks provided the optimum conditions for rock washout and drainage, fostering bauxite formation, and protected these deposits from later surface erosion (e.g., Bogatyrev et al. 2009; Mondillo et al. 2011; Mongelli et al. 2014). The bauxite genesis has been interpreted as an Oligocene–Miocene *in situ* bauxitization of precursor material of mixed origin, including sedimentary, metamorphic and magmatic (Šušnjara and Šćavničar 1976, 1978; Šušnjara et al. 1990). These interpretations were based predominantly on the bauxite heavy mineral assemblage, with the volcaniclastic origin inferred from predominant presence of euhedral prismatic zircons (e.g., in some horizons of the CK section more than 90% of the transparent heavy mineral grains are zircons; Šušnjara and Šćavničar 1976, 1978). Since zircons from SB volcaniclastic horizons (Šušnjara and Šćavničar 1974) are petrographically similar to bauxite zircons, and similar zircons are absent in the older bauxites, Upper Cretaceous karstified limestones and Paleogene deposits found in the region, the bauxite zircons have been interpreted as derived from the SB volcaniclastic rocks.

The Crveni Klanac (CK) section of strata, located in the southeastern margin of the SB, contains massive bauxites, bauxitic clays, clays and calcitic clays hosted in karstified Upper Cretaceous limestones, which underlie the lower SB lacustrine coal-bearing beds and marls with dreissenid bivalves (Fig. 1b, c; Šušnjara and Šćavničar 1976, 1978; Šušnjara et al. 1990). The ore deposit is bounded by faults, which caused the lowering of the relief and enabled bauxite accumulation in paleo-depression. The original size of the deposit was 200 x 150 m, with a maximum thickness of 30 m. Gibbsite, kaolinite, goethite and hematite are the principal CK bauxite mineralogy (Šušnjara et al. 1990).

Analytical methods

Six discrete bauxite horizons were identified and sampled from a 14.5 m thick CK bauxite deposit, as well as the overlying basal SB lacustrine unit (Fig. 2). The bauxite samples were characterized by a combination of bulk geochemical analyses, X-ray powder diffraction (XRPD) analysis of the whole-rock samples and fractions <4µm, optical and field emission scanning electron microscopy (FESEM) and *in situ* LA-ICP-MS U-Pb isotope analyses of accessory zircon, followed by high-precision CA-ID-TIMS U–Pb isotope analyses of the same, polished zircon crystals. High-precision U-Pb isotope analysis was also used for the analysis of zircons from SB oldest volcaniclastic horizon.

Bauxite mineralogy and geochemistry

X-ray diffraction (XRD)

The mineralogy of six bauxite whole rock samples and the <4 µm fractions of six bauxite samples were detected via X-ray powder diffraction (XRPD), using a Siemens D5000 diffractometer equipped with Cu tube (Cu-Kα radiation), automatic divergence slit, and graphite monochromator at the Department of Sciences, of the University of Basilicata (Italy). Random powders were used for the XRD analysis of the whole sample, within the diffraction range between 2° and 70° 2θ. Oriented aggregates were used for the XRD analysis of the <4 µm grain-size fraction, previously obtained by repeated Stokes' Law settling. For the oriented aggregates the 2° to 30° 2θ range was investigated and the analysis was carried out on air-dried, ethylene glycol solvated (overnight at 60 °C), and heated (at 550 °C for 2 h) specimens. The mineral phases identification was completed with X'Pert HighScore Plus software (PANalytical 2001) using the integrated PDF-4 (2006) database. The characterization of clay minerals was done following Moore and Reynolds (1989). To compare the examined samples, an estimation of whole sample mineral abundances were determined using the reference intensity ratios (RIR) listed in the aforementioned mineralogical database.

Optical and field emission scanning electron microscopy (FESEM)

Thin sections of the bauxite samples were studied by both transmitted and reflected light microscopy, in order to identify mineral phases and their textures. The thin sections of 3 samples, as well as their rock fragments, were analyzed by a Carl Zeiss Merlin FESEM with an Oxford energy-dispersive X-ray (EDS) detector at the University of Zaragoza (Spain). For this, the thin sections were previously carbon-coated. All other bauxite horizons, as well as microfacies of the overlying SB lacustrine limestones and marls, were studied petrographically at the Croatian Geological Survey (Zagreb, Croatia).

Compositional images of the samples were obtained using two types of backscattered electron detectors: angular selective (AsB) and energy selective (EsB). The accelerating voltage used for the AsB and EDS was 15 kV, with a beam current of 600 pA. For the ESB, the accelerating voltage was 4 kV with a beam current of 200-600 pA. Morphological images were also obtained from fragments of the rocks using a secondary electron detector (Inlens), using an accelerating voltage was 3-5 kV with a beam current of 100 pA. In addition, semi-quantitative analyses were carried out using the EDS detector in order to identify mineral chemistry with a detection limit of 0.1%.

Whole-rock geochemistry

Major, trace, and rare earth element (REE) concentrations of six bauxite whole-rock samples were determined by inductively coupled plasma–optical emission spectrometry (ICP-OES) and inductively coupled plasma–mass spectrometry (ICP–MS) at Bureau Veritas Commodities Canada Ltd. (Canada), following their standard procedures. Analytical uncertainties were less than ± 5%, except for elements at a concentration of 10 ppm or lower, for which uncertainties were ± 5–10%. Total loss on ignition (LOI) was determined gravimetrically after heating overnight at 950 °C.

For the purpose of discussion, the rare earth element (REEs) concentrations were normalized to Chondrite standard (McDonough and Sun 1995). The Ce and Eu anomalies were calculated as The Ce and Eu anomalies were calculated as $Ce/Ce^{*}= 2Ce_{ch}/\sqrt{(La_{ch}^{*}+Nd_{ch})}$ and $Eu/Eu^{*}= 2Eu_{ch}/\sqrt{(Sm_{ch}^{*}+Gd_{ch})}$, respectively, where the subscript “ch” refers to normalized values for chondrite. All relevant analytical data can be found in Supplementary Material 1.

Zircon geochronology

Laser Ablation-Inductively Coupled Plasma Mass Spectrometry (LA-ICP-MS)

First, the samples CK-1 (CKC-Bx3), CK-2 (CKSP-Bx2) and CK-5 (CKSS-Bx1) were crushed and sieved to <500 µm, and separated into a heavy and light fraction using Wilfley table. After the separation of the magnet fraction, the heavy fraction was passed through methylene iodide heavy liquids. Individual zircon grains were handpicked from the heavy non-magnetic fraction under a binocular microscope to obtain the largest variety of grain types (e.g. shape and size). Fifty to sixty zircons from bauxite samples were mounted in epoxy resin and polished to expose the interior domains of individual crystals. These mounts were then imaged by backscattered electron (BSE) and cathodoluminescence (CL) techniques using a scanning electron microscope JSM-6610 LV coupled with an Energy Dispersive X-Max Large Area Analytical Silicon Drifted Spectrometer (Oxford) and CL-detector at the University of Belgrade (Serbia). *In situ* LA-ICP-MS U-Pb isotope analyses were completed using a New Wave Research (NWR) Excimer 193 nm laser-ablation system attached to a Perkin-Elmer ELAN DRC-e quadrupole inductively coupled plasma-mass spectrometer at the Geological Institute of Bulgarian Academy of Science (Sofia, Bulgaria). An in-laboratory designed ablation cell with lowered position effects, a "squid" smoothing device, used an energy density of 7.5 J/cm-2, a repetition rate of 8 s, and ablation craters of 35 µm. The analyses were carried out in blocks of 20-22, using GJ1 zircon (Jackson et al. 2004) as a primary standard reference material (SRM) to correct for fractionation (2 analyses every 6 to 8 analyses), and finally Plesovice (Slama et al. 2008) and 91500 (Wiedenbeck et al. 1995, 2004) as a secondary SRM for controlling systematic errors. Spot analyses were carefully selected based on observation of BSE and CL images in order to avoid mineral inclusions. The results were calculated off-line using Iolite combined with VizualAge, in order to obtain ages and ratios corrected for instrumental drift and down-hole fractionation (Paton et al. 2010, 2011). During the two sessions of analyses in February and May 2020, the Plesovice SRM was measured at 338.9 ±1.7 Ma, and 91500 at 1065 ± 8 Ma, respectively (2s, decay-const. errs included; MSWD of concordance 0.01 and 0.1). All relevant analytical data for age calculations can be found in Supplementary Material 2.

Zircon U-Pb Chemical Abrasion-Isotope Dilution-Thermal Ionization Mass Spectrometry (CA-ID-TIMS)

In order to refine the age of euhedral zircons dated by LA-ICP-MS, samples CK-5 (CKSS-Bx1) and CK-2 (CKSP-Bx2) were selected for high-precision CA-ID-TIMS analysis. Following acquisition of LA-ICP-MS data, zircons with younger $^{206}Pb/^{238}U$ ages were removed from epoxy mounts with a metal tool. In some cases, grains fractured during removal and were then processed as individual sub-grain analyses; these are denoted with a letter following the zircon number. The sub-grains thus represent random fragments, in many cases one analysis would be from just the tip of a zircon (e.g., CKSS-Bx1 Z36b), while the paired analysis included the core (e.g., CKSS-Bx1 Z36a). The zircon grains and sub-grains were then individually annealed in a muffle furnace at 900 °C for 48 hours (Mundil et al. 2004). The annealed grains were then subjected to chemical abrasion at 210 °C for 12 hours in concentrated HF in individual 200 µl Savillex placed in a Parr digestion vessel (Mattinson 2005; Widmann et al. 2019). The abraded material was then transferred to a 3 mL Teflon beaker and leached on a hotplate at 80 °C in 6 N HCL overnight, followed by further cleaning through four rounds of 7 N HNO_3 in combination with ultrasonication. Individual cleaned zircon crystals were then loaded into individual 200 µl Savillex microcapsules, spiked with the EARTHTIME $^{202}Pb + ^{205}Pb + ^{233}U + ^{235}U$ tracer solution (calibration version 3; Condon et al. 2015; McLean et al. 2015) and dissolved with about 70 µl HF and trace HNO_3 in a Parr digestion vessel at 210 °C for 48 hours. Following dissolution, the samples were dried down and converted to a chloride by placing them back in the oven overnight in 6 N HCl. The samples were then dried down again and re-dissolved in 3 N HCl, and purified to U and Pb through anion exchange column chromatography (Krogh 1973). Once purified, the U and Pb fractions were combined in cleaned 7 ml Savillex beakers and dried down with trace H_3PO_4, prior to loading on outgassed zone-refined Re ribbon filaments with a Si-gel emitter.

Uranium and lead isotope analyses were completed on an Isotopx Phoenix TIMS machine at the University of Geneva (Switzerland). Lead measurements were made in dynamic mode using a Daly photomultiplier, and U was measured as an oxide in static mode using Faraday cups coupled to 10^{12} Ω resistors. The $^{18}O/^{16}O$ oxygen isotope ratio in uranium oxide was assumed to be 0.00205 based on previous measurements of the U500 standard. Mass fractionation of Pb and U was corrected using a $^{202}Pb/^{205}Pb$ ratio of 0.99506 and a $^{238}U/^{235}U$ ratio of 137.818 ± 0.045 (2σ) (Hiess et al. 2012). All common Pb was considered laboratory blank and was corrected using the long-termisotopic composition of the Pb blank at the University of Geneva. All data were processed with the Tripoli and Redux U–Pb software packages (Bowring et al. 2011; McLean et al. 2011). All ages were corrected for initial ^{230}Th disequilibrium in the melt using a magmatic U/Th ratio of 3.5. All relevant analytical data for age calculations can be found in Supplementary Material 3.

In order to better understand the onset of lacustrine deposition within the SB, and therefore constrain bauxite deposition, we also completed CA-ID-TIMS U-Pb zircon geochronology on sample LUČ-3 (Supplementary Material 3). This sample represents the oldest volcaniclastic rock within the SB, and was previously dated by Ar/Ar geochronology of biotite (de Leeuw et al. 2010, 2012; Šegvić et al. 2014). The methods for this sample were very similar to the bauxite grains, and are provided in detail in Brlek et al. (2020).

Results

Bauxite mineralogy, texture, morphology and geochemistry

X-ray diffraction (XRD)

The whole-rock XRD patterns are displayed in Fig. 3a, and the results of the semi-quantitative RIR analysis performed on these samples are presented in Fig. 2. Throughout the deposit, gibbsite and kaolinite are the predominant Al-bearing minerals, ranging in abundance from 7–45% and from 10–31%, respectively. Boehmite is also present in a few samples, and its concentration never exceeds 2%. Goethite and hematite are the principal Fe-bearing phases showing variable contents in different horizons. When these Fe-phases are both present, goethite is always more abundant then hematite, except in the sample CK-1. Calcite, anatase, rutile, 2:1 clay minerals, and gypsum complete the mineralogical association. Among these minerals, calcite shows very high and increasing contents towards the upper part of the section (e.g., 29% in CK-3, 60% in CK-5, and 82% in CK-6; Fig. 2). Other accessory minerals only have a minor presence (between 5% and trace). Further, quartz was detected in small quantities throughout the profile (e.g. up to 3% in sample CK-5). Allophane, imogolite and halloysite were not observed in any of the analyzed CK bauxite samples.

Results of the qualitative XRD analysis of oriented <4μm grain-size specimens indicate similar clay composition for all samples. In detail, comparing the air-dried, ethylene glycol-treated, and 550°C-heated patterns (Fig. 3b), the presence of kaolinite, which was also detected in the whole rock fractions, was further confirmed, and hydroxy-interlayered vermiculite was identified as the sole 2:1 clay mineral of the examined samples.

Optical and field emission scanning electron microscopy (FESEM)

The bauxite in samples CK-1 and CK-2 is characterized by a homogeneous texture in an optical microscope, with bauxite textures of a pelitomorphic to microgranular matrix (*sensu* Bárdossy 1982; Fig. 4a, b). The minerals of the fine-grained bauxite matrix of samples CK-1 and CK-2 were too small to be identified under optical microscope resolution (Fig. 4a, b). Occasionally, micron-sized oxides can be observed, and these are more abundant and larger in sample CK-2 (Fig. 4b). In samples CK-3 and CK-5, in contrast, euhedral to anhedral calcite crystals (sparite) are randomly distributed throughout the homogeneous bauxite matrix. The replacement of primary bauxite by calcite is observed in from sample CK-6, with previously homogeneous bauxite matrix occasionally embedded in microsparitic to sparitic matrix (Fig. 4c; see Durand et al. 2010). Additionally, the yellowish-brownish part of horizon CK-4 is characterized by fragmented and isolated bauxite matrix coated, surrounded, and rounded with Fe-oxide films (composition confirmed with FESEM investigation; Fig. 4d). Sparite also occurs in sample CK-4 as a yellowish-brownish infill, and displaces the primary bauxite homogeneous matrix (Fig. 4d).

Backscattered and secondary electron images show that samples CK-1 and CK-2 are composed of fine-grained homogeneous matrix with no laminations or other structures present. The matrix of the samples is mainly composed of kaolinite and gibbsite (Fig. 4e, f). Gibbsite has rounded morphologies and is consistently on a nanometer scale (Fig. 4e, f). Kaolinite crystals are heterometric, with subhedral to euhedral platy morphologies which occasionally show pseudohexagonal sections (Fig. 4e, f), and are larger in sample CK-2 (95nm–2μm) than in sample CK-1 (80nm–700nm). Kaolinite booklets are also recognized in both samples, and are up to 4 μm in diameter, and 3.5 μm in longitudinal development (Fig. 4g). The booklets observed in sample CK-2 have their sheets separated and they occasionally occur fractured. In addition, hematite crystals are observed between the booklets sheets in both samples. Some K-rich micas, somewhat broken and deformed, are also observed, with sizes from 25μm to 40μm. Micas occasionally have their sheets open and filled by kaolinite and gibbsite. Rounded nodules were observed, especially in sample CK-2, and are a mixture of clays and iron oxides. Iron and titanium oxides are likely hematite and rutile-anatase, based on XRD data. These minerals either form aggregates (16–100 μm), or are disseminated throughout the sample matrix as nanometer scale crystals, with occasional larger crystals (1-5 μm). Finally, CK-5 hosts anhedral to euhedral calcite (sparite, 10–150μm in size) in a fine-grained homogeneous matrix, composed of kaolinite and nanometric gibbsite with rounded morphologies (Fig. 4h, i). These kaolinite crystals are also heterometric, with platy morphologies that occasionally show pseudohexagonal sections (Fig. 4i). They are larger than those in the sample CK-1 and similar to those of the sample CK-2 (80nm–2μm). Kaolinite booklets are also observed and reach up to 14μm in diameter and 4μm in longitudinal development, and occasionally appear somewhat deteriorated (Fig. 4j).

Whole-rock geochemistry

The bauxite geochemistry has significant heterogeneity in major element composition (SiO_2 average=17.99±7.41; Al_2O_3 average= 24.93±12.73; Fe_2O_3 average=9.23±8.72; CaO average=15.69±18.43) (Fig. 2; Supplementary Material 1). Similar to the observation of calcite in several upper bauxite horizons, several samples are characterized by higher CaO concentrations (Fig. 2; Supplementary Material 1).

Similarly to major elements, concentrations of trace elements are highly heterogeneous, and have a strong correlative trends with CaO concentrations. The concentration of transition elements (Sc, V, Co, Ni, Cu, Zn), high field strength elements (hereafter HFSE; Ti, Zr, Nb, Hf, Ta,), and large ion lithophile elements (Rb, Cs, Ba, and Pb) all decrease with increasing CaO concentrations (Supplementary Material 1). The REE concentrations in the bauxite samples also parallel this trend, with the total abundance of REE's (ΣREE) decreasing in samples with increased CaO. Strontium is the exception to this trend in trace elements, as its concentration increases in samples with high CaO concentrations (Supplementary Material 1). The light REE to heavy REE fractionation index $(La/Yb)_{ch}$ (average=9.63±2.22) is close to that of the Upper Continental Crust ($(La/Yb)_{ch}$= 9.21, McLennan et al. 2006), similarly to Eu/Eu* index (0.67±0.02, Eu/Eu^*_{UCC}= 0.65) (Fig. 5a; Supplementary Material 1). Finally, the Ce/Ce* index is usually < 1 with the exception of the basal sample CK-1 (Ce/Ce* =1.62; Fig. 5a; Supplementary Material 1).

Elemental mobility during weathering is generally estimated assuming an element as immobile. Among the least mobile and most conservative elements during weathering, Ti can be assumed as largely immobile in karst bauxites (e.g. Mongelli et al. 2017 and references therein). With respect to Ti, Al and especially Si are largely depleted (Fig. 5b; Supplementary Material 1). Iron shows large fluctuations within a general trend of depletion, although it is enriched by ~25% in sample CK-4 (Fig. 5b; Supplementary Material 1).

Zircon geochronology

Laser Ablation-Inductively Coupled Plasma Mass Spectrometry (LA-ICP-MS)

The U-Pb LA-ICP-MS data are presented in Fig. 6 as well as in Supplementary Material 2, and $^{206}Pb/^{238}U$ zircon ages were used for interpretations of these data. The zircons from CK-5, CK-2 and CK-1 bauxite samples, from the highest, middle and lower bauxite horizons respectively, have similar age spectra. The youngest and highest abundance temporal populations are Miocene dates, mainly from 16 to 18.5 Ma, a secondary date peak of Oligocene grains (25-34 Ma), and several Eocene dates of 35-37 Ma (Fig. 6). Inherited cores and older zircon grains yield predominantly Early Paleozoic dates 440-500 Ma, with several Devonian (370-380 Ma) or Permian-Carboniferous dates (270-320 Ma; Fig. 6). The weighted mean $^{206}Pb/^{238}U$ ages of the youngest zircon populations are indistinguishable at the level of uncertainty: 16.56 ± 0.68 Ma (CK-5; n = 5), 16.50 ± 0.43 Ma (CK-2; n = 7) and 16.47 ± 0.58 Ma (CK-1; n = 6).

Zircon U-Pb Chemical Abrasion-Isotope Dilution-Thermal Ionization Mass Spectrometry (CA-ID-TIMS)

Thorium-corrected $^{206}Pb/^{238}U$ zircon date determinations are used for all interpretations of CA-ID-TIMS data, because this chronometer provides the most precise and accurate values for rocks of this age (Figs. 7, 8; Supplementary Materials 3–6). The stratigraphically highest bauxite horizon CK-5 (CKSS-Bx1) yielded seven concordant Miocene dates, two normally discordant dates which plot near the Miocene in Concordia space, two older concordant dates (86.33 Ma and 265.29 Ma), and four older normally discordant dates (Figs. 7, 8; Supplementary Materials 3, 5, 6). Concordant Miocene zircon dates ranged from 16.953 ± 0.032 Ma to 18.587 ± 0.073 Ma, with overlapping dates at 16.96 and 17.13 Ma (Fig. 8). High-precision analyses of the middle bauxite unit CK-2 (CKSP-Bx2) yielded fourteen concordant Miocene zircon dates and two older concordant dates (30.535 and 376.57 Ma) (Figs. 7, 8; Supplementary Materials 3, 4). Miocene zircon ranged from 16.960 ± 0.023 Ma to 18.347 ± 0.040 Ma, with multiple overlapping dates at approximately 16.96 and 17.21 Ma (Fig. 8). Finally, individual zircon grains from LUČ-3, a volcaniclastic rock located in the basal region of Miocene lacustrine rocks in the SB, yielded dates ranging from 17.307 ± 0.022 to 19.309 ± 0.044 Ma, with three grains yielding overlapping dates at 17.31 Ma (Fig. 8; Supplementary Material 3).

Discussion

Formation of CK bauxites: insights from mineralogy and geochemistry

Massive, homogeneous karst bauxites represent the dominant style of bauxite in the CK profile, with the CK-4 horizon being a heterogeneous exception (Fig. 2). The homogeneous texture of almost all bauxite horizons, with pelitomorphic to microgranular matrices, is highly indicative of an authigenic origin of the massive bauxites (*sensu* Bárdossy 1982). Gibbsite and kaolinite, the predominant CK bauxite mineral phases (Figs. 2–4), are typical bauxite minerals. Electron microscopy shows that the CK bauxites have a fine-grained matrix of kaolinite and gibbsite, with minor proportions of hematite, goethite and rutile-anatase (Fig. 4) (Bardossy 1982; Bardossy and Combes 1999). The rounded nodules in samples CK-1 and CK-2 indicate that edaphic characteristics are recorded in both samples, as these nodules could be considered as pisoid precursors (Tilley 1994). The subhedral to euhedral and occasional pseudohexagonal morphologies of the platy kaolinite crystals of the bauxite matrix indicate that kaolinite is authigenic and not detrital, since erosion and transport processes would have modified them (Fig. 4; e.g., Bauluz et al. 2014; Yuste et al. 2015, 2020; Laita et al. 2020). The kaolinite booklets are also indicative of an authigenic origin, as this morphology is not robust enough to survive any significant transport. Furthermore, the apparent growth of kaolinite and gibbsite between the sheets of detrital micas also suggests that both kaolinite and gibbsite have been formed *in situ*. Therefore, the association of authigenic phases, such as kaolinite and gibbsite associated with Fe and Ti oxides, suggests that all were formed *in situ* as a consequence of the edaphic process that enabled the autochtonous bauxite formation (e.g., Bauluz et al. 2014; Yuste et al. 2015, 2020). These bauxites and their representative mineral associations formed during warm and humid tropical and sub-tropical climate that promoted intense chemical weathering with the dissolution of primary silicate minerals (e.g., the observed micas) and crystallization of aluminium-rich phases and oxides (Muggler et al. 2007; Eggleton et al. 2008; Fernández-Caliani and Cantano 2010; Huang et al. 2012; Bauluz et al. 2014; Yuste et al. 2015, 2020; Singh et al. 2018). In contrast, the largest-sized kaolinite booklets, which occasionally have sheets which are separated and broken (Fig. 4), seem to have undergone minor transport due to potential reworking processes. Fragmentation of homogeneous bauxite matrix with formation of Fe-oxide films and coatings around and including the isolated matrix parts in the CK-4 horizon (Fig. 4), can also be interpreted as an *in situ* process, that took place either during the process of bauxitization or subsequently during diagenesis (Bárdossy 1982; see also Achyuthan and Fedoroff 2008; Yuste et al. 2015, 2020; Laita et al. 2020).

The field observations agree with mineralogical and geochemical data: the amount of calcite in the bauxite horizons increases upward throughout the CK section (Fig. 2). The occurrence of authigenic carbonate throughout the profile, with the notable exception of the basal horizons (CK-1 and CK-2), indicates that diagenetic modification may affect bauxite (as previously suggested by Šušnjara et al. 1990; Figs. 2, 3; Supplementary Material 1). Carbonate precipitation in the supracrustal environment depends on the aqueous matrix, particularly solute contents, pH, Eh, and P_{CO2} (e.g., Kirk et al. 2015 and references therein). Neogene sediments overlying bauxites are lacustrine limestones and marls, where secondary calcite likely precipitated from percolating water during lacustrine sedimentation, filling voids and displacing homogeneous bauxite matrix (especially CK-4 and CK-6 horizons; Fig. 4; Bárdossy 1982; Laita et al. 2020; see also Wang et al. 1994 and Durand et al. 2010). The groundmass of soils and sediments affected by diagenesis commonly hosts isolated calcite crystals with rhombohedral to acicular morphology, such as those observed in horizons CK-3, CK-4 and CK-5 (Fig. 4). This suggests a period of stable environmental and geological conditions, which promoted low nucleation density and slow growth of calcite (Mees and Van Ranst 2011).

The geochemistry of the CK bauxite samples also leads to significant interpretations concerning the CK bauxite formation and its post-genetic modifications. The (La/Yb)ch values of the bauxite samples which were affected by carbonate addition (CK-2 to CK-6: average $(La/Yb)_{ch}$=9.40±2.41) are close to that of basal CK-1 sample which was not affected by diagenetic modifications ($(La/Yb)_{ch}$=10.77) (Fig. 5a). Furthermore, the samples have $(La/Yb)_{ch}$ values similar to the average upper continental crust ($(La/Yb)_{ch}$= 9.21, McLennan et al. 2006) (Fig. 5a). This suggests that later percolating water, which caused carbonate precipitation, did not affect the $(La/Yb)_{ch}$ geochemistry associated to bauxitization, and implies that prevailing alkaline pH soil solution affected the Crveni Klanac section from the bauxitization to the carbonate addition (Pourret et al. 2010). The Ce/Ce* index has been largely used in order to track the paleo-redox evolution during bauxitization, as cerium enrichment and positive Ce anomalies is driven by oxidation (e.g., Mongelli et al. 2014; Khosravi et al. 2017). The basal horizon (CK-1) has a positive Ce anomaly (Fig. 5a), suggesting oxidation and precipitation of cerianite (CeO_2), according to a well-documented mechanism in karst bauxites (e.g., Abedini et al. 2020). In the other parts of the section which were affected by diagenetic modifications, the Ce anomaly is always <1 (Fig. 5a), indicating that the redox conditions either promoting cerium oxidation, or the stability of cerianite, during bauxitization did not occur.

Although carbonate successions host karst bauxite deposits, the dissolution of carbonate bedrock is not considered suitable for the formation of karst bauxite, and instead, a large variety of protoliths likely contributed material for bauxitization (e.g., Comer 1974; Bárdossy 1982; Bárdossy and Combes 1999; Abedini et al. 2020 and references therein). Among the several proxies used to identify the parent rock(s) of karst bauxites, the Eu anomaly (an index of chemical differentiation affected by minor fractionation during intense weathering) is commonly used order to elucidate the parental material of karst bauxite deposits (e.g., Mongelli et al. 2014, 2016; Khosravi et al. 2017; Sinisi 2018; Abedini et al. 2020). The samples from the CK section have similar Eu/Eu* values (Eu/Eu*: 0.67 ± 0.02, n=6), which is close to the upper continental crust composition (UCC: Eu/Eu*=0.65; Post Archean Australian Shales: Eu/Eu*=0.66; Taylor and McLennan 1985), and therefore it is likely that the same protolith(s) contributed the Al-rich detritus throughout the development of the various horizons of the CK bauxite. The heavy mineral assemblage of these bauxites includes staurolite, andalusite, kyanite, garnet and zircon (Šušnjara and Šćavničar 1976, 1978), and therefore detritus incorporated in the formation of the CK bauxites had to involve multiple sources, including magmatic, metamorphic and sedimentary rocks. Therefore, although CK bauxites show a broad consistence of the average Eu/Eu* values with the Miocene volcaniclastic deposits of the SB (and regional Carpathian-Pannonian Region; e.g., Šegvic et al. 2014; Lukács et al. 2018; Brlek et al. 2020), these rocks cannot be confirmed nor excluded as being the dominant CK bauxite precursor material, in accordance with a mechanism that was suggested for other (Cretaceous) karst bauxites of the Mediterranean region that involves volcanic ash (Mondillo et al. 2011; Boni et al. 2013; Putzolu et al. 2018). Instead, based on currently available data, a combination of Oligocene–Miocene volcaniclastic material and siliciclastic detritus (Mongelli et al. 2014, 2016; Sinisi 2018) represents a more realistic model for CK precursor material.

High-precision zircon geochronology

Age interpretation of Sinj Basin volcaniclastic rocks

Individual zircon dates from the volcaniclastic horizon from the SB range over 2 Ma, and yield an MSWD in excess of that expected for a single population at the level of precision, and therefore require interpretation to determine the eruption age of this rock. It is common for high silica rocks to incorporate a moderate to high load of antecrystic and xenocrystic zircon, which may host autocrystic overgrowths and therefore have euhedral appearances based on their recent magmatic history (e.g., Lipman and Bachman 2015; Gonzales 2015; Samperton et al. 2015; Rosera et al., accepted). While Pb-loss could artificially extend the age spectra by yielding young ages, a 12-hour chemical abrasion has been demonstrated as a robust measure to limit Pb-loss, and was used in this work (Widmann et al. 2019). Therefore, we interpret that the youngest population of zircon in this sample reflects the age of final crystallization, with older grains representing a mix of antecrystic and xenocrystic zircons (e.g., Wotzlaw et al. 2018; Szymanowski et al. 2019; Gaynor et al. 2019; Ellis et al. 2019; Brlek et al. 2020; Rosera et al., accepted). The weighted mean and uncertainty for this interpretation is 17.312 ± 0.015/0.016/0.024 Ma for LUČ-3 (Fig. 8; 2σ uncertainty given as: internal only/internal with tracer calibration/internal, tracer calibration and with ^{238}U decay constant). Previous ^{40}Ar/^{39}Ar geochronology of this volcaniclastic deposit, intercalated within the lowest lacustrine unit of the SB, indicated it was deposited at 17.91 ± 0.18 (de Leeuw et al. 2010, 2012). Our new age is approximately 600 ka younger than the previous biotite geochronology suggesting that deposition of lacustrine sediments did not begin as early as previously interpreted.

Interpreting zircon age spectra and maximum depositional ages (MDA's) in CK bauxites

Zircon age spectra in all three samples analyzed via LA-ICP-MS (CK-1, CK-2 and CK-5) is dominated by Miocene analyses (16 to 18.5 Ma), with a lesser, secondary peak in the Oligocene (25–34 Ma and a few Late Eocene ages) (Fig. 6; Supplementary Material 2). Volcanic and volcaniclastic rocks, representing the products of regional Late Eocene to earliest Miocene volcanism, are recorded both in the Balkan Peninsula (including the Inner Dinarides) as well as in the vicinity of the Periadriatic Fault Zone (Fig. 1a; Pamić and Balen 2001; Schefer et al. 2011; Cvetković et al. 2016; Kelemen et al. 2017, 2020), and could represent the sources of predominantly Oligocene zircon dates recorded in CK bauxites. The Miocene CK bauxite zircons targeted by individual grain and sub-grain analyses by CA-ID-TIMS of the upper two bauxites (CK-2 and CK-5) reveals a more complex distribution of dates within the Early Miocene zircon domains; these analyses yield a spectra with high zircon age scatter (Figs. 7, 8; Supplementary Material 3). Both the LA-ICP-MS and CA-ID-TIMS data reveal the presence of inherited, xenocrystic components in these Miocene zircons that potentially inhibit the direct translation of the zircon date to the timing of the magmatic system it formed within. While *in situ* analyses have an advantage when dealing with inherited cores, LA-ICP-MS is limited by both precision and accuracy relative to CA-ID-TIMS (e.g., Schaltegger et al. 2015; Herriott et al. 2019). Therefore, in order to overcome this zircon inheritance, we prescreened the grains using SEM and LA-ICP-MS prior to ID-TIMS, in some cases also doing sub-grain analyses, and we subsequently base much of our interpretations of the bauxite U-Pb zircon data based upon these CA-ID-TIMS data. These analyses indicate either: (1) that the Early Miocene (i.e., ~17–18.5 Ma) zircon detritus is mostly sourced from several regional Early Miocene volcanic events and/or a heterogeneous suite of local volcaniclastic material (e.g., Pécskay et al. 2006; de Leeuw et al. 2010, 2012; Šegvić et al. 2014; Lukács et al. 2018; Brlek et al. 2020), or (2) that the protolith for these bauxite horizons was predominately an individual regional eruption event and/or individual local Miocene volcaniclastic deposit with complicated zircon geochronology.

There are a host of regional volcanic events as well as local volcaniclastic rocks that could have potentially provided zircons matching the ages sampled in this study, and therefore contributed the protolith material to the depositional zone of the bauxites (see also Kelemen et al. 2017, 2020). The Carpathian-Pannonian Region, located in the northeastern part of the Alpine–Mediterranean region of eastern Central Europe, hosted compositionally diverse, post-collisional magmatism over the last 20 Ma (Pécskay et al. 2006; Seghedi and Downes 2011). This extension-related volcanism started with the eruption of the silicic pyroclastic rocks during the Early Miocene, highlighted by the eruption of regional-scale ignimbrites at 18.060 ± 0.012 Ma, 17.5 ± 0.3 Ma, 17.05 ± 0.055 Ma and 16.816 ± 0.059 Ma (Lukács et al. 2018; Brlek et al. 2020; Fig. 1a). There are volcaniclastic rocks in other intra-montane lacustrine basins (DLSB) proximal to the SB, including a horizon previously dated at 17.00 ± 0.17 Ma via Ar/Ar in the nearby Livno Basin (de Leeuw et al. 2012 and references therein). Importantly, there are Lower–Middle Miocene volcaniclastic rocks intercalated throughout the SB lacustrine succession within ~30 km of the CK bauxite location that have been interpreted as sourced from the Carpathian-Pannonian Region (Šušnjara and Šćavničar 1974; de Leeuw et al. 2010; Šegvić et al. 2014; Fig. 1a). The zircon geochronology from LUČ-3, one of the lowermost SB volcaniclastic rocks, has significant overlap in the zircon dates of the bauxite samples, and therefore may have contributed detritus for bauxite formation (Fig. 8). This would require contributions from additional volcanic horizons however, as the bauxites have a significant population of zircons younger than any found in LUČ-3. There are multiple other units that have been identified as being intercalated within the basal SB lacustrine unit that are stratigraphically younger than LUČ-3 (Šegvić et al. 2014), and could therefore contribute further zircon, and protolith material to the CK bauxites. In this scenario it is probable that one of these as yet undated events would represent the zircon population that defines the MDA of the CK precursor material. As illustrated by the zircon age distributions within LUČ-3, it should also be considered that any single unit within the SB would not only carry zircon that capture the eruption age, but also antecrystic zircon that can capture zircon growth that can be many 100s ka prior to the eruption age. These complex zircon age spectra could be further mixed between volcaniclastic units prior to being sequentially washed into the final CK depositional zone, providing the complexity in age distributions with a low probability of sampling the zircon relating to the 'youngest' units within the bauxites.

The alternative hypothesis is that the complex age range in the CK bauxite samples is a function of igneous processes and a large xeno- and antecrystic crystal cargo in a single volcanic eruption and/or volcaniclastic unit that was sequentially deposited in the CK depositional zone and was the dominant source of Miocene zircon. Due to the mixing of xenocrystic, antecrystic and autocrystic zircon crystallization within individual mineral grains and then averaged by whole grain dissolution, individual ignimbrite eruptions dated with CA-ID-TIMS can reveal concordant zircon ages with >1 Ma of protracted zircon dates within individual eruptive events (e.g., Wotzlaw et al. 2013; Szymanowski et al. 2019; Ellis et al. 2019).Therefore, a single ignimbrite eruption could reasonably yield protracted ranges in zircon dates similar to the samples dated in this study. It is possible that the old ages reflect a xenocrystic component in a relatively homogeneous igneous source material for the bauxite horizons, rather than a mixed detrital input. CA-ID-TIMS analyses indicate that there are normally discordant grains with Miocene $^{206}Pb/^{238}U$ ages, which suggests subtle components of inheritance present in some grains. More reliable provenance reconstructions require building a large database of geochronological data for the region, both for bauxite deposits and potential volcanic sources, as well as application of additional proxies, such as zircon petrochronology (e.g., Liu et al. 2014; Szymanowski et al. 2016, 2019; Ellis et al. 2019; Lu et al. 2019).

Regardless of the nature of the detrital source of the volcanic material, both samples dated by CA-ID-TIMS have consistent, indistinguishable dates at the youngest identified ages in each sample, and therefore we interpret that these dates are not outliers resulting from Pb-loss, but capturing the primary zircon crystallization ages, and therefore the maximum depositional age (MDA) for the protolith and the maximum bauxite formation age. The weighted mean value of the youngest population of zircons in each sample yields an MDA of 16.955 ± 0.013/0.014/0.023 Ma (n = 2; MSWD = 0.013) for CK-5 (CKSS-Bx1) and 16.960 ± 0.014/0.015/0.023 Ma (n = 3; MSWD = 0.14) for CK-2 (CKSP-Bx2) (Fig. 8). All five of the analyses interpreted to determine MDA's for the two samples are analytically a single age population (16.9576 ± 0.0096/0.011/0.021 Ma; n = 5; MSWD = 0.15), indicating that while CK-5 is younger due to stratigraphic relationships, an absolute age difference between the formation of the two horizons is unresolvable using our zircon dates.

As mentioned above, it is not uncommon for high silica magmatism to crystallize zircon with an abundance of xenocrystic components, and this may not be readily observed during SEM imagery. Whole grain analyses, as commonly done in U-Pb ID-TIMS geochronology, may bias the accuracy of individual dates, and yielding artificially older ages in some geological settings. While this method does not allow for replicate analyses when compared to breaking the grain evenly (e.g., Heriott et al. 2019), for samples ranging from those with subtle antecrystic cores to those with obvious xenocrystic cores these young exterior zircon domains represent the most precise, accurate target for MDA's. Therefore, we suggest that subsequent studies which require strong temporal control using MDA's consider utilizing sub-grain ID-TIMS analyses in order to generate the most accurate high-precision ages.

Model and duration of bauxite formation, implications for SB evolution and climatic implications

The Upper Cretaceous limestones hosting CK bauxite deposits belong to the Adriatic-Dinaridic Carbonate Platform (Tari-Kovačić 1994; Mandic et al. 2008). With the start of the compressional tectonics during the Eocene, the platform turned into a foredeep with deposition of flysch and molasses (Promina Formation), and was subsequently subaerially exposed during the Oligocene (Mandic et al. 2008). Accordingly, these basement rocks could have begun to undergo the combined effects of tectonic deformation, erosion and weathering beginning in the Oligocene (perhaps even from Late Eocene), allowing for the gradual development of the karstified paleo-depressions suitable for trapping bauxite precursor material (Šušnjara et al. 1990; see also Bárdossy 1982; Bogatyrev et al. 2009). Based on geochronological and geochemical data, the same protoliths provided the bauxite precursor material for all CK bauxite horizons. CK bauxite geochronology (Fig. 6) seems to be consistent with the regional geological framework: the euhedral zircons of Oligocene (and Late Eocene) age probably represent the initial volcanic material to have reached the newly formed pre-Miocene paleorelief and accumulated in the paleo-depressions, with accumulation of new material, including younger volcanic zircon, up until the Early Miocene.

Our provided high-precision maximum depositional age (MDA) of 16.9576 ± 0.0096/0.011/0.021 Ma (Fig. 8) of the CK bauxite parent material provide chronologic constraint on the bauxite parent material true depositional age and on the maximum age of bauxite formation. The bauxite precursor detritus appears to be relatively homogenized throughout the CK profile based on similar geochemistry, mineralogy and zircon age spectra (Figs. 6, 7), and was subjected to autochtonous bauxitization.

At the time of the maximum bauxitization age (~17 Ma), certain areas of the SB basement were still exposed, specifically the Upper Cretaceous limestones hosting the Miocene bauxites in the southeastern region of the SB. This is in contrast with previous work, which interpreted that lacustrine environments had covered the entirety of the SB by this point, based on 17.91 Ma Ar/Ar geochronology of a volcanic horizon intercalated in lacustrine sediments (LUČ-3; de Leeuw et al. 2010, 2012). Our revision of this date indicates that SB lacustrine sedimentation in the northern portion of the basin began at 17.312 ± 0.024 Ma (Fig. 8). This volcaniclastic horizon occurs intercalated only with variously colored marls in the northwestern part of the basin (Fig. 1), however the lower SB stratigraphy is comprised of coal-bearing beds and marls with dreissenid bivalves overlying Miocene bauxites in the southeastern part of the basin (Fig. 1; Šušnjara and Sakač 1988; Šušnjara et al. 1990; Mandic et al. 2008; de Leeuw et al. 2010). Although the two types of sedimentary rocks of the basal unit of the SB have been interpreted as synchronous, lateral transitions or contacts between the two have not been observed in the field (Šušnjara and Sakač 1988). Therefore, while lacustrine environments existed in the northwestern part of the SB by 17.3 Ma, there was still subaerial exposure in the southeastern portion of the basin. This implies there was significant paleorelief in the SB during Early Miocene, and that the lacustrine flooding across the SB was diachronous, with flooding first in the northwest and later in the southeast.

The minimum age of bauxite formation can be inferred by stratigraphic relationships and Ar/Ar dating within the SB. Since there is no high-precision geochronological data for the lower SB stratigraphy in the southeastern portion of the basin overlying the CK bauxites, we instead rely on a 16.24 Ma using $^{40}Ar/^{39}Ar$ sanidine date from an overlying lacustrine section of the middle SB stratigraphy to provide a minimum age for bauxitization (LUČ-2; de Leeuw et al. 2010, 2012). These upper and lower age constraints indicate that bauxitization must have taken place in 700 ka or less (Fig. 9), which agrees with the estimated 10^5–10^6 years required to develop strong oxisols, soil analogues for bauxites, and the formation timeframes of ancient bauxites during tropical and subtropical humid weathering (Retallack 2001, 2010; Bogatyrev et al. 2009; Huang et al. 2012; Retallack et al. 2016). This age range coincides remarkably with the onset and the early stage of the Miocene Climatic Optimum (MCO; Fig. 9; Kasbohm and Schoene 2018; Methner et al. 2020; Sosdian et al. 2020), implying that the *in situ* bauxitization in mid-latitude European areas occurred during the Cenozoic period of elevated atmospheric CO_2 levels and global warming.

Correlation of CK bauxite formation to the Miocene Climatic Optimum

The MCO represents the 14.7–17 Ma warm period (sustained global warmth ~3–4 °C warmer than present) interrupting long-term Cenozoic cooling and declining pCO_2 levels, and reduced continental ice volume (Fig. 9; e.g., Kasbohm and Schoene 2018; Methner et al. 2020; Sosdian et al. 2020). The MCO is a part of the Monterey carbon isotope excursion (MCIE) - a prolonged ~1.0 ‰ positive carbon isotope excursion ($\delta^{13}C$) of the global oceans (e.g., Zachos et al. 2001; Holbourn et al. 2015; Sosdian et al. 2020). There is a growing evidence for elevated and variable pCO_2 levels of 350 to 630 ppm during the MCO global warm period (e.g., Kasbohm and Schoene 2018; Methner et al. 2020; Sosdian et al. 2020; see also Retallack 2009). The MCO may therefore have similarities in the magnitude of global change we are currently observing in the present-day, with rise in global atmospheric pCO_2, global temperature and decrease in polar ice volume, and therefore is crucial to better understand (e.g., Retallack 2009; Kasbohm and Schoene 2018; Methner et al. 2020; Sosdian et al. 2020).

Although continental paleoclimate records from the MCO are essential for assessing past global climate change, they are far less common than the available marine record (Methner et al. 2020). The 15.7 Ma old lateritic bauxites (Oxisols) developed on Columbia River Basalts (CRB, weathered to bauxite to depths of 18m) in western Oregon (and Washington) in the United States have been directly correlated to the MCO (Fig. 9; e.g., Liu et al. 2013, Retallack et al. 2016). In contrast, the contemporaneous intra-basaltic Alfisols in eastern Oregon have been interpreted to reflect that local rainfall variations could have also determined the local expressions of weathering during MCO (e.g., Sheldon et al. 2003; Retallack 2010; Retallack et al. 2016). Intense chemical weathering of Vogelsberg basalts (central Germany) during MCO is held responsible for lateritic bauxite development in these mid-latitude European areas (Figs. 1, 9; 51° paleolatitude; Schwarz 1997; Retallack 2010). Formation of terrestrial kaolin deposits trapped in Transdanubian Range (Pannonian Basin, Hungary) Miocene karstic sinkholes was interpreted as partially related to *in situ* weathering of wind-borne material (mainly tephra) during the MCO (Figs. 1, 9; Kelemen et al. 2020). Optimum climatic conditions during MCO also stimulated lake formation in the Dinarides (Mandic et al. 2020 and references therein). The high relative percentage of warm pollen taxa (thermophilous plants) throughout the SB lacustrine stratigraphy is indicative of a warm subtropical and a yearlong humid climate for this area (in accordance with other European areas) during Early and early Middle Miocene (Jiménez-Moreno et al. 2008 and references therein).

Although the temporal and causative relationships between the CRB and the MCO is still debated, and there are still outstanding concerns regarding the most reliable age models for climate proxy records across the MCO, it is generally accepted that the MCO began at approximately 17 Ma (Kasbohm and Schoene 2018; Methner et al. 2020; Sosdian et al. 2020; Fig. 9). The onset of the MCO is not clearly resolved in North Alpine Foreland Basin (NAFB, Switzerland; Fig. 1) paleosols, however, the timing of central European warming agrees with the onset of the MCO at high latitudes between 17.4 and 16.9 Ma, and the NAFB paleosol carbonates indicate (based on clumped isotope data) there was a warming period between 17.4 and 16.6 Ma (Methner et al. 2020; Fig. 9). The peak of MCO-related warming was 30.6 °C at 16.59 Ma, with temperature declining to 23.4 °C by 16.38 Ma, and terrestrial temperatures remained below 25 °C between 16.4 and 15.8 Ma, coinciding with the Miocene cooling interval (Methner et al. 2020; Fig. 9). This first warming peak recorded in NAFB paleosols correlates with climatic evidence in other regional and global terrestrial and marine environments, such as increased $\delta^{13}C$ marine carbonate values after 16.7 Ma and increased pCO_2 levels (e.g., Holbourn et al. 2015; Methner et al. 2020 and references therein). Although this timing is 400 ka later than the reconstructed maximum bottom water temperatures recorded at ~17.0 Ma, it correlates well with the timing of minimum global ice volume (Lear et al. 2015; Methner et al. 2020).

MCO-related CK bauxitization provides an independent evaluation of paleotemperature and paleorainfall calculations at comparable latitudes in Europe during the ~700 ka during which the CK bauxites formed, which indicate elevated mean annual temperatures (MAT) and mean annual precipitation (MAP). In NAFB (southern Germany; Fig. 1), during the Karpatian period (17 to ~16.3 Ma), the MAT and MAP values (based on silicified woods) had a range from 15.7 to 20.5 °C and from 1138 to 1355 mm, respectively (Fig. 9; e.g., Böhme et al. 2007, 2011; Bruck et al. 2007, 2011). Pollen-based data from the SB and the larger DLSB indicate that the Early Miocene had a warm subtropical and humid climate, favorable for bauxite formation (Jiménez-Moreno et al. 2008). In order for *in situ* bauxitization to occur, the temperatures must have been warmer than 17–22°C, with more than 1100–1200 mm of annual precipitation, which gives direct paleoclimate constraints to mid-latitude European continental settings during the early stages of the MCO (Fig. 9; Bárdossy 1982; Bárdossy and Combes 1999; Bogatyrev et al. 2009; Retallack 2008, 2010; Mondillo et al. 2011). Along with agreeing with reconstructions of climatic conditions during the onset and the early stages of the MCO, CK bauxites provide a distinct geochronological constraint on the onset and the early stages of the MCO in European continental settings, and a unique insight into prevailing conditions during Early Miocene in parts of southeastern Europe (central Dalmatia; Fig. 9).

Conclusions

New zircon geochronology data, integrated with compositional, mineralogical and morphological data from central Dalmatian (CK section) karst bauxites provide a unique insight into their genesis and formation. The subhedral to euhedral morphologies of the kaolinite crystals, together with gibbsite, are the predominant mineral phase of the bauxite homogeneous matrix, and these morphologies indicate that they are authigenic. Their *in situ* formation, a consequence of the edaphic process under prevailing alkaline pH conditions based on $(La/Yb)_{ch}$ values, indicates that the CK massive karstic bauxites are autochtonous. The presence of authigenic calcite throughout the profile, together with geochemical data, indicate that diagenetic modification affected these bauxites. *In situ* LA-ICP-MS zircon age spectra of the lower, middle and upper parts of the CK bauxite are very similar, dominated by Miocene (16 to 18.5 Ma) and Oligocene (25-34 Ma) ages, and together with similar geochemistry throughout the profile we interpret that all of the CK bauxite horizons have the same precursor materials. Individual zircon and sub-grain analyses by CA-ID-TIMS also revealed protracted Miocene zircon age spectra of the CK bauxites, as well as MDA of 16.9576 ± 0.0096/0.011/0.021 Ma of the CK bauxite parent material. In addition, zircon geochronology of a volcaniclastic horizon from the northeastern portion of the Sinj Basin (SB) indicates that there was significant paleorelief within the basin during the Early Miocene, and that lacustrine flooding across the SB was diachronous.

The MDA for bauxite parental material, which also serves as the maximum age of autochtonous bauxitization, coincides with the onset of the MCO. Based on currently available geochronological constraints, the maximum timeframe for CK bauxitization was less than ~700 ka. Continental proxies from several European mid-latitude areas indicate that there was a warming period between approximately 17–16.3 Ma, correlating with climatic evidence archived in regional and global terrestrial and marine environments. More than simply aligning with regional and local reconstructions of continental climatic conditions during the onset and the early stages of the MCO, the CK autochtonous bauxites provide a precise climatic constraint. In order for *in situ* bauxitization to have occurred, the mean annual temperature must have been higher than 17–22°C, with more than 1,100–1,200 mm of precipitation per year between 16.95–16.24 Ma in some southeastern parts of mid-latitude continental Europe. High-quality data provided in this study strengthen the view that periods of unusually widespread bauxite formation, beyond their modern distribution within the tropics, is correlated with times of global high warmth and precipitation, such as the MCO.

References

Abedini A, Rezaei Azizi M, Dill HG (2020) Formation mechanisms of lanthanide tetrad effect in limestone: an example from Arbanos district, NW Iran. Carbonates and Evaporites 35:1–16

Achyuthan H, Fedoroff N (2008) Ferricretes in Tamil Nadu, Chennai, South-Eastern India: from landscape to micromorphology, genesis, and paleoenvironmental significance. In: Kupur S, Stoops G (eds) New Trends in Soil Micromorphology. Springer-Verlag, Berlin-Heidelberg, pp 111–136

Bárdossy, G., 1982. Karst Bauxites. Bauxite Deposits on Carbonate Rocks. Elsevier, Amsterdam.

Bárdossy G, Combes PJ (1999) Karst bauxites: interfingering of deposition and palaeoweathering. Special Publication International Association of Sedimentologists 27:189–206

Bauluz B, Yuste A, Mayayo MJ, Canudo JI (2014) Early kaolinization of detrital Weald facies in the Galve Sub-basin (Central Iberian Chain, north-East Spain) and its relationship to palaeoclimate. Cretaceous Research 50:214–227

Bogatyrev BA, Zhukov VV, Tsekhovsky YuG (2009) Formation conditions and regularities of the distribution of large and superlarge bauxite deposits. Lithology and Mineral Resources 44:135–151

Böhme M, Bruch AA, Selmeier A (2007) The reconstruction of Early and Middle Miocene climate and vegetation in Southern Germany as determined from the fossil wood flora. Palaeogeography Palaeoclimatology Palaeoecology 253:91–114

Böhme M, Winklhofer M, Ilg A (2011) Miocene precipitation in Europe: Temporal trends and spatial gradients. Palaeogeography Palaeoclimatology Palaeoecology 304:212–218

Boni M, Rollinson G, Mondillo N, Balassone G, Santoro L (2013) Quantitative mineralogical characterization of karst bauxite deposits in the Southern Apennines, Italy. Economic Geology 108:813–833

Bowring JF, McLean NM, Bowring AA (2011) Engineering cyber infrastructure for U-Pb geochronology: Tripoli and U-Pb_Redux. Geochemistry Geophysics, Geosystems, v. 12

Brlek M, Kutterolf S, Gaynor S, Kuiper K, Belak M, Brčić V, Holcová K, Wang K-L, Bakrač K, Hajek-Tadesse V, Mišur I, Horvat M, Šuica S, Schaltegger U (2020) Miocene syn-rift evolution of the North Croatian Basin (Carpathian-Pannonian Region): new constraints from Mts. Kalnik and Požeška gora volcaniclastic record with regional implications. International Journal of Earth Sciences 109:2775–2800

Bruch AA Uhl D, Mosbrugger V (2007) Miocene climate in Europe—patterns and evolution: a first synthesis of NECLIME. Palaeogeography Palaeoclimatology Palaeoecology 253:1–7

Bruch AA, Utescher T, Mosbrugger V (2011) Precipitation patterns in the Miocene of Central Europe and the development of continentality. Palaeogeography Palaeoclimatology, Palaeoecology 304:202–211

Comer JB (1974) Genesis of Jamaican bauxite. Economic Geology 69:1251–1264

Condon DJ, Schoene B, McLean NM, Bowring SA, Parrish RR (2015) Metrology and traceability of U–Pb isotope dilution geochronology (EARTHTIME Tracer Calibration Part I): Geochimica et Cosmochimica Acta 164:464–480

Cvetković V, Šarić K, Pécskay Z, Gerdes A (2016) The Rudnik Mts. volcano-intrusive complex (central Serbia): An example of how magmatism controls metallogeny. Geologia Croatica 69:89–99

de Leeuw A, Mandic O, Vranjković A, Pavelić D, Harzhauser M, Krijgsman W, Kuiper KF (2010) Chronology and integrated stratigraphy of the Miocene Sinj Basin (Dinaride Lake System, Croatia). Palaeogeography Palaeoclimatology Palaeoecology 292:155–167

de Leeuw A, Mandic O, Krijgsman W, Kuiper K, Hrvatović H (2012) Paleomagnetic and geochronologic constraints on the geodynamic evolution of the Central Dinarides. Tectonophysics 530/531:286–298

Durand N, Monger HC, Canti MG (2010) Calcium carbonate features. In: Stoops G, Marcelino V, Mees F (eds) Interpretation of Micromorphological Features of Soils and Regoliths. Elsevier, Amsterdam, pp 149–194

Eggleton RA, Taylor G, Le Gleuher M, Foster LD, Tilley DB, Morgan CM (2008) Regolith profile, mineralogy and geochemistry of the Weipa Bauxite, northern Australia. Australian Journal of Earth Sciences 55:17–43

Ellis BS, Schmitz MD, Hill M (2019) Reconstructing a Snake River Plain “super-eruption” via compositional fingerprinting and high-precision U/Pb zircon geochronology. Contributions to Mineralogy and Petrology 174:101

Fernández-Caliani JC, Cantano M (2010) Intensive kaolinization during a lateritic weathering event in South-West Spain. Mineralogical and geochemical inferences from a relict paleosol. Catena 80:23–33

Gaynor SP, Rosera JM, Coleman DS (2019) Intrusive history of the Oligocene Questa porphyry molybdenum deposit, New Mexico. Geosphere 15:548–575

Gehrels G (2014) Detrital zircon U-Pb geochronology applied to tectonics. Annual Review of Earth and Planetary Sciences 42, pp 127–149

Gonzales DA (2015) New U-Pb zircon and ^{40}Ar/^{39}Ar age constraints on the late Mesozoic to Cenozoic plutonic record in the Western San Juan Mountains. The Mountain Geologist 52:5–42

Herriott TM, Crowley JL, Schmitz MD, Wartes MA, Gillis RJ (2019) Exploring the law of detrital zircon: LA-ICP-MS and CA-TIMS geochronology of Jurassic forearc strata, Cook Inlet, Alaska, USA. Geology 47:1044–1048

Hiess J, Condon DJ, McLean N, Noble SR (2012) ^{238}U/^{235}U systematics in terrestrial uranium-bearing minerals. Science 335:1610–1614

Holbourn AE, Kuhnt W, Kochhann KGD, Andersen N, Meier KJS (2015) Global perturbation of the carbon cycle at the onset of the Miocene Climatic Optimum. Geology 43:123–126

Huang PM, Li Y, Sumner ME (eds) (2012) Handbook of Soil Sciences: Properties and Processes, second ed. CRC Press, Taylor & Francis Group, Boca Raton

Jackson S, Pearson N, Griffin W, Belousova E (2004) The application of laser ablation-inductively coupled plasma-mass spectrometry to in situ U-Pb zircon geochronology. Chemical Geology 211:47–69

Jiménez-Moreno G, Mandic O, Harzhauser M, Pavelić D, Vranjković A (2008) Vegetation and climate dynamics during the early Middle Miocene from Lake Sinj (Dinaride Lake System, SE Croatia). Review of Palaeobotany and Palynology 152:237–245

Kasbohm J, Schoene B (2018) Rapid eruption of the Columbia River flood basalt and correlation with the mid-Miocene climate optimum. Science Advances 4

Kelemen P, Dunkl I, Csillag G, Mindszenty A, von Eynatten H, Józsa S (2017) Tracing multiple resedimentation on an isolated karstified plateau: the bauxite-bearing Miocene red clay of the Southern Bakony Mountains, Hungary. Sedimentary Geology 358:84–96

Kelemen P, Csillag G, Dunkl I, Mindszenty A, Kovács I, von Eynatten H, Józsa S (2020) Terrestrial kaolin deposits trapped in Miocene karstic sinkholes on planation surface remnants, Transdanubian Range, Pannonian Basin (Hungary). Geological Magazine. https://doi.org/10.1017/S0016756820000515

Khosravi M, Abedini A, Alipour S, Mongelli G (2017) The Darzi-Vali bauxite deposit, West-Azarbaidjan Province, Iran: critical metals distribution and parental affinities. Journal of African Earth Sciences 129:960–972

Kirk GJD, Versteegen A, Ritz K, Milodowski AE (2015) A simple reactive transport model of calcite precipitation in soils and other porous media. Geochimica et Cosmochimica Acta 165:108–122

Korbar T (2009) Orogenic evolution of the External Dinarides in the NE Adriatic Region: a model constrained by tectonostratigraphy of Upper Cretaceous to Paleogene carbonates. Earth-Science Reviews 96:296–312

Krogh TE (1973) A low-contamination method for hydrothermal decomposition of zircon and extraction of U and Pb for isotopic age determinations. Geochimica et Cosmochimica Acta 37:485–494

Laita E, Bauluz B, Aurell M, Bádenas B, Canudo JI, Yuste A (2020) A change from warm/humid to cold/dry climate conditions recorded in lower Barremian clay-dominated continental successions from the SE Iberian Chain (NE Spain). Sedimentary Geology 403:105673

Lear CH, Coxall HK, Foster GL, Lunt DJ, Mawbey EM, Rosenthal Y, Sosdian SM, Thomas E, Wilson PA (2015) Neogene ice volume and ocean temperatures: Insights from infaunal foraminiferal Mg/Ca paleothermometry. Paleoceanography 30:1437–1454

Lipman PW, Bachmann O (2015) Ignimbrites to batholiths: Integrating perspectives from geological, geophysical, and geochronological data. Geosphere 11, 705–743.

Liu X-M, Rudnick RL, McDonough WF, Cummings ML (2013) Influence of chemical weathering on the composition of the continental crust: Insights from Li and Nd isotopes in bauxite profiles developed on Columbia River Basalts. Geochimica et Cosmochimica Acta 115:73–91

Liu J, Zhao Y, Liu A, Zhang S, Yang Z, Zhuo S (2014) Origin of Late Palaeozoic bauxites in the North China Craton: constraints from zircon U–Pb geochronology and *in situ* Hf isotopes. Journal of the Geological Society 171:695–707

Liu X, Mao X, Yuan Y, Ma M (2019) Aeolian accumulation: An alternative origin of laterite on the Deccan Plateau, India. Palaeogeography Palaeoclimatology Palaeoecology 518:34–44

Lu G, Di Capua A, Winkler W, Rahn M, Guillong M, von Quadt A, Willett SD (2019) Restoring the source-to-sink relationships in the Paleogene basins in the Central and southern Alps (Switzerland, Italy, France): a detrital zircon study approach. International Journal of Earth Sciences 108:1817–1834

Lukács R, Harangi S, Guillong M, Bachmann O, Fodor L, Buret Y, Dunkl I, Sliwinski J, von Quadt A, Peytcheva I, Zimmerer M (2018) Early to Mid-Miocene syn-extensional massive silicic volcanism in the Pannonian

Basin (East-Central Europe): Eruption chronology, correlation potential and geodynamic implications. Earth-Science Reviews 179:1–19

Mandic O, Pavelić D, Harzhauser M, Zupanič J, Reischenbacher D, Sachsenhofer RF, Tadej N, Vranjković A (2008) Depositional history of the Miocene Lake Sinj (Dinaride Lake System, Croatia): a long-lived hard-water lake in a pull-apart tectonic setting. Journal of Paleolimnology 41:431–452

Mandic O, Harzhauser M, Neubauer TA (2020) Taxonomy, palaeoecology and stratigraphy of the middle Miocene mollusk fauna from the Gračanica coal pit near Bugojno in Bosnia and Herzegovina. Palaeobiodiversity and Palaeoenvironments 100:519–549

Mattinson JM (2005) Zircon U–Pb chemical abrasion (“CA-TIMS”) method: combined annealing and multi-step partial dissolution analysis for improved precision and accuracy of zircon ages. Chemical Geology 220:47–66

McDonaugh WF, Sun SS (1995) The composition of the Earth. Chemical Geology 67:1050–1056

McLean NM, Bowring JF, Bowring SA (2011) An algorithm for U–Pb isotope dilution data reduction and uncertainty propagation. Geochemistry Geophysics Geosystems 12:Q0AA18

McLean NM, Condon DJ, Schoene B, Bowring SA (2015) Evaluating uncertainties in the calibration of isotopic reference materials and multi-element isotopic tracers (EARTHTIME Tracer Calibration Part II). Geochimica et Cosmochimimica Acta 164:481–501

McLennan SM, Taylor SR, Hemming SR (2006) Composition, differentiation and evolution of continental crust: constrains from sedimentary rocks and heat flow. In: Brown M, Rushmer T (ed) Evolution and Differentiation of The Continental Crust. Cambridge University Press, Cambridge, pp 92–134

Mees F, Van Ranst E (2011) Euhedral sparitic calcite in buried surface horizons in lake basins, southwestern Kalahari, Namibia. Geoderma 163:109–118

Methner, K., Campani, M., Fiebig, J., Löffler, N., Kempf, O., Mulch, A., 2020. Middle Miocene long-term continental temperature change in and out of pace with marine climate records. Nature 10:7989.

Mindszenty A (2016) Bauxites: Feedbacks of System Earth at Greenhouse times. Geologia Croatica 69:79–87

Mondillo N, Boni M, Balassone G, Rollinson G (2011) Karst bauxites in the Campania Apennines (southern Italy): a new approach. Periodico di Mineralogia 80:407–432

Mongelli G, Boni M, Buccione R, Sinisi R (2014) Geochemistry of the Apulian karst bauxites (southern Italy): chemical fractionation and parental affinities. Ore Geoloy Reviews 63:9–21

Mongelli G, Buccione R, Gueguen E, Langone A, Sinisi R (2016) Geochemistry of the apulian allochthonous karst bauxite, Southern Italy: Distribution of critical elements and constraints on Late Cretaceous Peri-Tethyan palaeogeography. Ore Geology Reviews 77:246–259

Mongelli G, Boni M, Oggiano G, Mameli P, Sinisi R, Buccione R, Mondillo N (2017) Critical metals distribution in Tethyan karst bauxite: The Cretaceous Italian ores. Ore Geology Reviews 86:526–536

Moore DM, Reynolds RC Jr (1989) X-ray diffraction and the identification and analysis of clay minerals, second ed. Oxford University Press, New York

Muggler CC, Buurman P, van Doesburg JDJ (2007) Weathering trends and parent material characteristics of polygenetic oxisols from Minas Gerais, Brazil: I. Mineralogy. Geoderma 138:39–48

Mundil R, Ludwig KR, Metcalf I, Renne PR (2004) Age and timing of the Permian mass extinctions: U/Pb dating of closed-system zircons. Science 305:669–673

Pamić J, Balen D (2001) Tertiary magmatism of the Dinarides and the adjoining South Pannonian Basin: an overview. Acta Vulcanologica 13:9–24

Paton C, Woodhead JD, Hellstrom JC, Hergt JM, Greig A, Maas R (2010) Improved laser ablation U‐ Pb zircon geochronology through robust downhole fractionation correction. Geochemistry Geophysics Geosystems 11:Q0AA06

Paton C, Hellstrom J, Bence P, Woodhead J, Hergt J(2011) Iolite: Freeware for the visualisation and processing of mass spectrometric data, Journal of Analytical Atomic Spectrometry 26:2508–2518

Pécskay Z, Lexa J, Szakács A, Seghedi I, Balogh K, Konečný V, Zelenka T, Kovacs M, Póka T, Fülöp A, Márton E, Panaiotu C, Cvetković V (2006) Geochronology of Neogene magmatism in the Carpathian arc and intra-Carpathian area. Geologica Carpathica 57:511–530

Pourret O, Gruau M, Dia A, Davranche M, Molénat J (2010) Colloidal control on the distribution of rare earth elements in shallow groundwaters. Aquatic Geochemistry 16:31–59

Putzolu F, Papa AP, Mondillo N, Boni M, Balassone G, Mormone A (2018) Geochemical characterization of bauxite deposits from the Abruzzi mining district (Italy). Minerals 8:298

Retallack GJ (2001) Soils of the past: An introduction to paleopedology, second ed. Blackwell Science, Oxford

Retallack GJ (2008) Cool-climate or warm-spike lateritic bauxites at high latitudes?. The Journal of Geology 116:558–570

Retallack GJ (2009) Refining a pedogenic-carbonate CO_2 paleobarometer to quantify a middle Miocene greenhouse spike. Palaeogeography Palaeoclimatology Palaeoecology 281:57–65

Retallack GJ (2010) Lateritization and Bauxitization Events. Economic Geology 105:655−667

Retallack GJ, Gavin DG, Davis EB, Sheldon ND, Erlandson JM, Reed MH, Bestland EA, Roering JJ, Carson RJ, Mitchell RB (2016) Oregon 2100: projected climatic and ecological changes. University of Oregon Museum of Natural History Bulletin 26:1–21

Rosera JM, Gaynor SP, Coleman DS accepted. Spatio-temporal shifts in magmatism and mineralization in northern Colorado beginning in the late Eocene. Economic Geology

Samperton KM, Schoene B, Cottle JM, Keller CB, Crowley JL, Schmitz MD (2015) Magma emplacement, differentiation and cooling in the middle crust: Integrated zircon geochronological-geochemical constraints from the Bergell intrusion, Central Alps. Chemical Geology 417:322–340

Schaltegger U, Schmitt AK, Horstwood MSA (2015) U-Th-Pb zircon geochronology by ID-TIMS, SIMS and laser ablation ICP-MS: Recipes, interpretations, and opportunities. Chemical Geology 402:89–110

Schefer S, Cvetković V, Fügenschuh B, Kounov A, Ovtcharova M, Schaltegger U, Schmid SM (2011) Cenozoic granitoids in the Dinarides of southern Serbia: age of intrusion, isotope geochemistry, exhumation history and significance for the geodynamic evolution of the Balkan Peninsula. International Journal of Earth Sciences 100:1181–1206

Schwarz T, (1997) Lateritic bauxite in central Germany and implications for Miocene palaeoclimate. Palaeogeography Palaeoclimatology Palaeoecology 129:37–50

Seghedi I, Downes H (2011) Geochemistry and tectonic development of Cenozoic magmatism in the Carpathian-Pannonian region. Gondwana Research 20:655–672

Sharman GR, Malkowski MA (2020) Needles in a haystack: Detrital zircon U-Pb ages and the maximum depositional age of modern global sediment. Earth-Science Reviews 203:103109

Sheldon ND (2003) Pedogenesis and geochemical alteration of the Picture Gorge subgroup, Columbia River basalt, Oregon. Geological Society of America Bulletin 115:1377–1387

Singh BP, Srivastava VK (2018) Petrographical, mineralogical, and geochemical characteristics of the Palaeocene lateritic bauxite deposits of Kachchh Basin, Western India. Geological Journal 54:2588–2607

Sinisi R (2018) Mineralogical and geochemical features of Cretaceous bauxite from San Giovanni Rotondo (Apulia, Southern Italy): A provenance tool. Minerals 8:567

Slama J, Kosler J, Crowley JL, Gerdes A, Hanchar J, Horstwood M, Morris GA, Nasdala L, Norberg N, Schaltegger U, Tubrett MN, Whitehouse MJ (2008) Plešovice zircon - a new natural reference material for U-Pb and Hf isotopic microanalysis. Chemical Geology 249:1–35

Sosdian SM, Babila TL, Greenop R, Foster GL, Lear CH (2020) Ocean Carbon Storage across the middle Miocene: a new interpretation for the Monterey Event. Nature 11:134

Szymanowski D, Ellis BS, Wotzlaw JF, Buret Y, von Quadt A, Peytcheva I, Bindeman IN, Bachmann O (2016) Geochronological and isotopic records of crustal storage and assimilation in the Wolverine Creek-Conant Creek system, Heise eruptive centre, Snake River Plain. Contributions to Mineralogy and Petrology 171:106

Szymanowski D, Ellis BS, Wotzlaw J-F, Bachmann O (2019) Maturation and rejuvenation of a silicic magma reservoir: High-resolution chronology of the Kneeling Nun Tuff. Earth and Planetary Science Letters 510:103–115

Šegvić B, Mileusnić M, Aljinović D, Vranjković A, Mandic O, Pavelić D, Dragičević I, Mählmann RF (2014) Magmatic provenance and diagenesis of Miocene tuffs from the Dinaride Lake System (the Sinj Basin, Croatia). European Journal of Mineralogy 26:83–101

Šušnjara A, Šćavničar B (1974) Tufovi u neogenskim naslagama srednje Dalmacije (južna Hrvatska). Geološki vjesnik 27:239–253

Šušnjara A, Šćavničar B (19769 Akcesorni teški minerali u boksitima i karbonatnim stijenama podine boksita. IV jugoslavenski simpozijum o istraživanju i eksploataciji boksita, Hercegnovi, pp 53–66

Šušnjara A, Šćavničar B (1978) Heavy minerals as provenance indices of tertiary bauxites in Dalmatia (Yugoslavia). 4th International Congress for the Study of Bauxites, Alumina and Aluminium ICSOBA 2, Athens, pp 822–837

Šušnjara A, Sakač K (1988) Miocenski slatkovodni sedimenti područja Sinja u sredjoj Dalmaciji. Geološki vjesnik 41:51–74

Šušnjara A, Sakač K, Gabrić A, Šinkovec B (1990) Boksiti područja Sinja u Srednjoj Dalmaciji. Geološki vjesnik 43:169–179

Tari-Kovačić V (1994) The role of palaeogene clastics in the tectonic interpretation of Northern Dalmatia. Geologia Croatica 47:127–138

Taylor SR, McLennan AM (1985) The Continental Crust: Its Composition and Evolution. Blackwell, Oxford

Tilley DB (1994) Models of bauxitic pisolith genesis: data from Weipa, Queensland. PhD thesis, Australian National University, Canberra

van Unen M, Matenco L, Nader FH, Darnault R, Mandic O, Demir V (2019) Kinematics of foreland-vergent crustal accretion: inferences from the Dinarides evolution. Tectonics 38:49–76

Wang Y, Nahon D, Merino E (1994) Dynamic model of the genesis of calcretes replacing silicate rocks in semi-arid regions. Geochimica et Cosmochimica Acta 58:5131–5145

Widmann P, Davies JHFL., Schaltegger U (2019) Calibrating chemical abrasion: Its effects on zircon crystal structure, chemical composition and U-Pb age. Chemical Geology 511:1–10

Wiedenbeck M, Allé P, Corfu F, Griffin WL, Meier M, Oberli F, von Quadt A, Roddick JC, Spiegel W (1995) Three natural zircon standards for U-Th-Pb, Lu-Hf, trace element and REE analyses. Geostandards Newsletter 19:1–23.

Wiedenbeck M, Hanchar JM., Peck WH., Sylvester P, Valley J, Whitehouse M, Kronz A, Morishita Y, Nasdala L, Fiebig J, Franchi I, Girard J-P, Greenwood RC, Hinton R, Kita N, Mason PRD, Norman M, Ogasawara M, Piccoli PM, Rhede D, Satoh H, Schulz-Dobrick B, Skår Ø, Spicuzza MJ, Terada K, Tindle A, Togashi S, Vennemann T, Xie Q, Zheng Y-F (2004) Further characterisation of the 91500 zircon crystal. Geostandards and Geoanalytical Research 28:9–39

Wotzlaw J-F, Schaltegger U, Frick DA, Dungan MA, Gerdes A, Günther D (2013) Tracking the evolution of large-volume silicic magma reservoirs from assembly to supereruption. Geology 41:867–870

Wotzlaw J-F, Brack P, Storck J-C (2018) High-resolution stratigraphy and U-Pb geochronology of the Middle Triassic Buchenstein Formation (Dolomites, northern Italy): precession-forcing of hemipelagic carbonate sedimentation and calibration of the Anisian-Ladinian boundary interval. Journal of the Geological Society 175:71–85

Zachos J, Pagani M, Sloan L, Thomas E, Billups K (2001) Trends, rhythms, and aberrations in global climate 65 Ma to present. Science 292:686–693

Zupanič J, Babić Lj (2011) Sedimentary evolution of an inner foreland basin margin: Palaeogene Promina Beds of the type area, Mt. Promina (Dinarides, Croatia). Geologia Croatica 64:101–119

Yuste A, Bauluz B, Mayayo MJ (2015) Genesis and mineral transformations in lower Cretaceous karst bauxites (NE Spain): climatic influence and superimposed processes. Geological Journal 50:839–857

Yuste A, Camacho I, Bauluz B, Mayayo MJ, Laita E (2020) Palaeoweathering events recorded on siliciclastic continental deposits (Albian, Lower Cretaceous) in NE Spain. Applied Clay Science 190:105598

Figure captions

Fig.1 a Geographical position of the Sinj Basin (SB) and Dinaride Lake System Basins. The position of volcanic and volcaniclastic rocks representing the products of regional Late Eocene to Early Miocene volcanic episodes, as well as locations of continental mid-latitude central European Miocene Climatic Optimum (MCO) records, is also provided. **b**, **c**: Schematized geological map (**b**) and generalized stratigraphic columns (**c**; lower and middle units) of the SB (modified after Šušnjara and Sakač, 1988; de Leeuw et al., 2010; Šegvić et al., 2014), with positions of some Miocene bauxite localities and SB Lower Miocene volcaniclastic rocks. Subdivision and lithostratigraphic units according to Šušnjara and Sakač (1988).

Fig. 2 Vertical section (geological column) of the Crveni Klanac (CK) section, represented by variously colored massive bauxite horizons (CK-1, CK-2, CK-3, CK-5) and CK-4 horizon with films and coatings, hosted in the Upper Cretaceous limestones and overlain by the lower SB lacustrine deposits. Variations in bulk mineralogical content and geochemical composition throughout the bauxite profile are shown.

Fig. 3 Whole-rock (**a**) and clay fraction (**b**) XRPD patterns obtained from CK bauxite samples (from the bottom horizon CK-1 to the top horizon CK-6). Ant = anatase; Bhm = boehmite, Cal = calcite, Gbs = gibbsite, Gt = goethite, Hem = hematite, HIV = hydroxy-interlayered vermiculite, Kln = kaolinite, Qtz = quartz, Rt = rutile.

Fig. 4 Transmitted light optical microscopy (**a**–**d**) and FESEM (E–J) images of CK bauxite samples. **a**, **b** Homogeneous bauxite texture of samples CK-1 and CK-2 composed of pelitomorphic to microgranular matrix, with micron-sized Fe oxides (**b**). Parallel nicols. **c** Replacement of primary bauxite by calcite (sample CK-6) with previously homogeneous bauxite matrix embedded in microsparitic to sparitic matrix. Crossed nicols. **D** The yellowish-brownish part of the horizon CK-4 with fragmented and isolated bauxite matrix coated, surrounded and rounded with Fe-oxide films. Sparite infilling voids can also be observed. Parallel nicols. **e**, **f** Secondary electron images showing subhedral to euhedral kaolinite crystals and gibbsite with rounded morphology composing the CK-1 and CK-2 bauxite homogeneous matrix. **g** Backscattered electron image of kaolinite booklets in sample CK-1. **h** Backscattered electron image showing anhedral to euhedral calcite (sparite) in a fine-grained homogeneous bauxite matrix (sample CK-5). **i** Secondary electron image showing heteromorphic kaolinite crystals with platy morphologies and nanometric gibbsite with rounded morphologies composing homogeneous matrix of the sample CK-5. **j** Backscattered electron image showing somewhat deteriorated kaolinite booklets of the sample CK-5. Hem = hematite, Gib = gibbsite, Kln = kaolinite, Cal = calcite

Fig. 5 **a** $(La/Yb)_{ch}$ and Ce/Ce* values, as indicators of pH of the soil solution and paleo-redox conditions, respectively, of the bauxite samples affected at various degree by carbonate addition. **b** Mobility of the chemical elements as change % relatively to the Upper Continental Crust composition and assuming Ti as an immobile element. See text for further details.

Fig. 6 Probability distribution function (PDF) graphs of $^{206}Pb/^{238}U$ LA-ICP-MS zircons dated in this study, highlighting that age spectra from all three dated samples are dominated by Early Miocene zircon analyses, with a subordinate peak in the Early Oligocene.

Fig. 7 SEM imagery of zircons dated using CA-ID-TIMS in this study. All ages are Th-corrected $^{206}Pb/^{238}U$ ages, and individual grains or subgrains which yielded normally discordant ages are indicated with a blue *. All zircons were previously analyzed by LA-ICP-MS, and had a significant volume of material ablated from the grain prior to CA-ID-TIMS and therefore the volume of zircon analyzed by CA-ID-TIMS is less than shown here. Grains which were fractured during removal from the LA-ICP-MS mount and analyzed separately are denoted with a red line which indicates where they broke, and which portion of the grain refers to individual ages. Grains most commonly fractured along the laser ablation pits.

Fig. 8 Rank order plot of ID-TIMS Th-corrected $^{206}Pb/^{238}U$ ages from Miocene-aged detrital zircon hosted in CK bauxite horizons, and volcanic zircon from sample LUČ-3, an ash bed intercalated within the lower lacustrine unit of the SB. Unfilled boxes/data points represent $^{206}Pb/^{238}U$ age of normally discordant analysis. See text for discussion of how these ages are interpreted.

Fig. 9 Compilation of Crveni Klanac (CK) *in situ* bauxitization and other continental mid-latitude Miocene Climatic Optimum (MCO) records (modified from Methner et al., 2020). **a** Statistical onset of the MCO and the duration of the subsequent Middle Miocene Climatic Transition (MMCT; after Methner et al., 2020). **b** MCO (orange) and MMCT (blue) in Central Europe as inferred by Methner et al., 2020. **c** Geochronological constraints on the timing of the onset and the maximum timeframe for the CK bauxitization, with implied mean annual temperatures (MAT) and mean annual precipitation (MAP) in southeastern parts of mid-latitude continental Europe (central Dalmatia) during MCO (this study). **d** Clumped isotope temperature record (pedogenic carbonate) and paleofloral-based MAT of the North Alpine Foreland Basin (NAFB; Böhme et al., 2007; Methner et al., 2020). **e** Other Central European and North American mid-latitude records of intense chemical weathering during MCO (CGLB, Central German lateritic bauxites – Schwarz, 1997; TBR kd, Transdanubian range kaolin deposits – Kelemen et al., 2020; CRB bx, Columbia River Basalts lateritic bauxites – Liu et al., 2013).

Electronic Supplementary Material captions

Supplementary Material 1

ICP geochemistry table

Supplementary Material 2

LA-ICP-MS geochronology table

Supplementary Material 3

CA-ID-TIMS geochronology table

Supplementary Material 4

Miocene Concordia of the CK-2 bauxite horizon

Supplementary Material 5

Miocene Concordia of the CK-5 bauxite horizon

Supplementary Material 6

Full Concordia of the CK-5 bauxite horizon

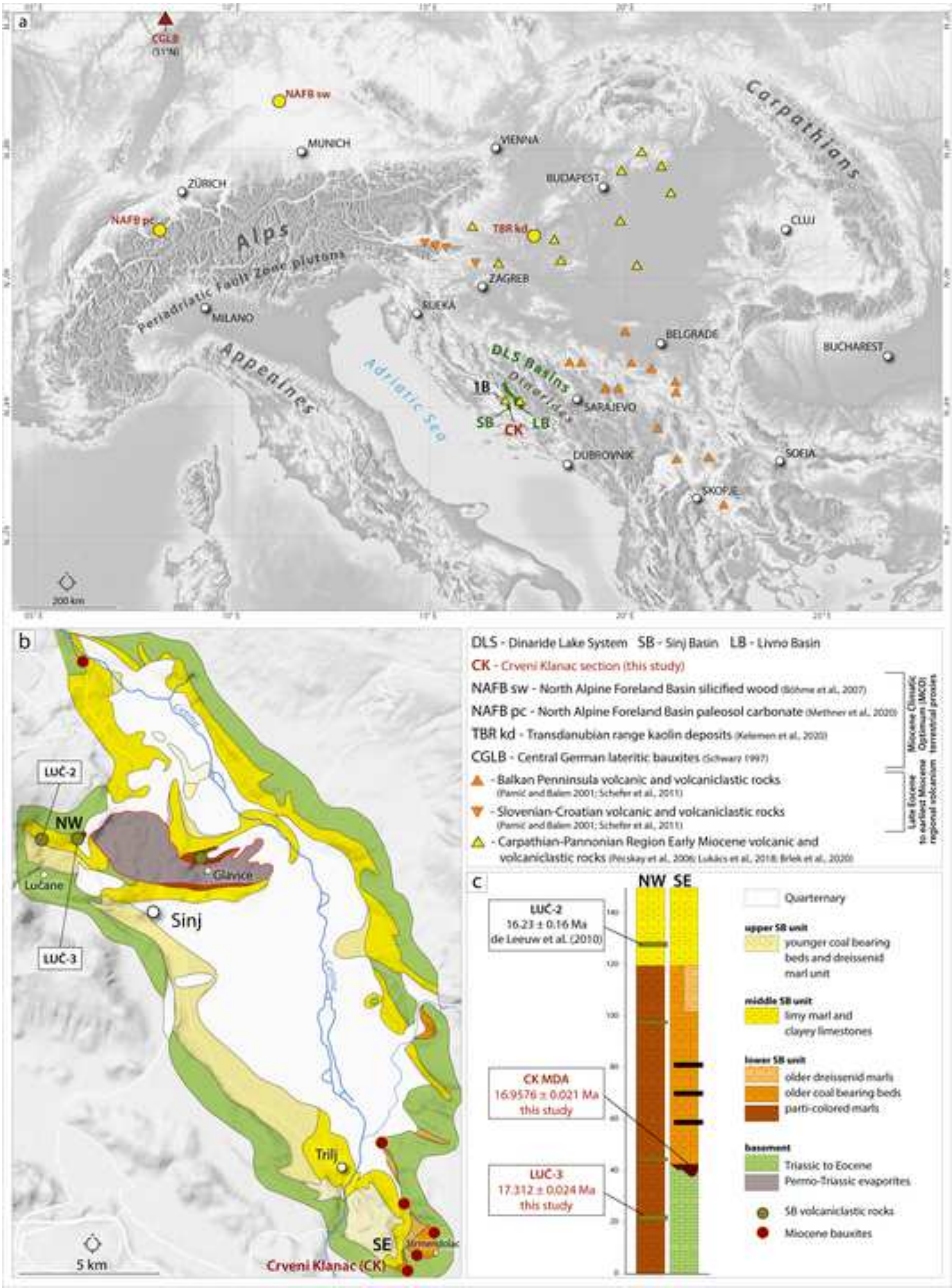
a
CGLB
(51°N)
NAFB sw
MUNICH
VIENNA
Carpathians
ZÜRICH
BUDAPEST
NAFB pc
Alps
TBR kd
CLUJ
Periadriatic Fault Zone plutons
ZAGREB
MILANO
RIJEKA
BELGRADE
BUCHAREST
Appenines
Adriatic Sea
DLS Basins
Dinarides
IB
SB
CK
LB
SARAJEVO
DUBROVNIK
SOFIA
SKOPJE
200 km
b
LUČ-2
NW
Lučane
Glavice
Sinj
LUČ-3
Trilj
SE
Strmendolac
Crveni Klanac (CK)
5 km
DLS - Dinaride Lake System SB - Sinj Basin LB - Livno Basin
CK - Crveni Klanac section (this study)
NAFB sw - North Alpine Foreland Basin silicified wood (Böhme et al., 2007)
NAFB pc - North Alpine Foreland Basin paleosol carbonate (Methner et al., 2020)
TBR kd - Transdanubian range kaolin deposits (Kelemen et al., 2020)
CGLB - Central German lateritic bauxites (Schwarz 1997)
Miocene Climatic Optimum (MCO) terrestrial proxies
▲ - Balkan Penninsula volcanic and volcaniclastic rocks (Pamić and Balen 2001; Schefer et al., 2011)
▼ - Slovenian-Croatian volcanic and volcaniclastic rocks (Pamić and Balen 2001; Schefer et al., 2011)
△ - Carpathian-Pannonian Region Early Miocene volcanic and volcaniclastic rocks (Pécskay et al., 2006; Lukács et al., 2018; Brlek et al., 2020)
Late Eocene to earliest Miocene regional volcanism
c
NW SE
LUČ-2
16.23 ± 0.16 Ma
de Leeuw et al. (2010)
CK MDA
16.9576 ± 0.021 Ma
this study
LUČ-3
17.312 ± 0.024 Ma
this study
140
120
100
80
60
40
20
0
Quarternary
upper SB unit
younger coal bearing beds and dreissenid marl unit
middle SB unit
limy marl and clayey limestones
lower SB unit
older dreissenid marls
older coal bearing beds
parti-colored marls
basement
Triassic to Eocene
Permo-Triassic evaporites
SB volcaniclastic rocks
Miocene bauxites

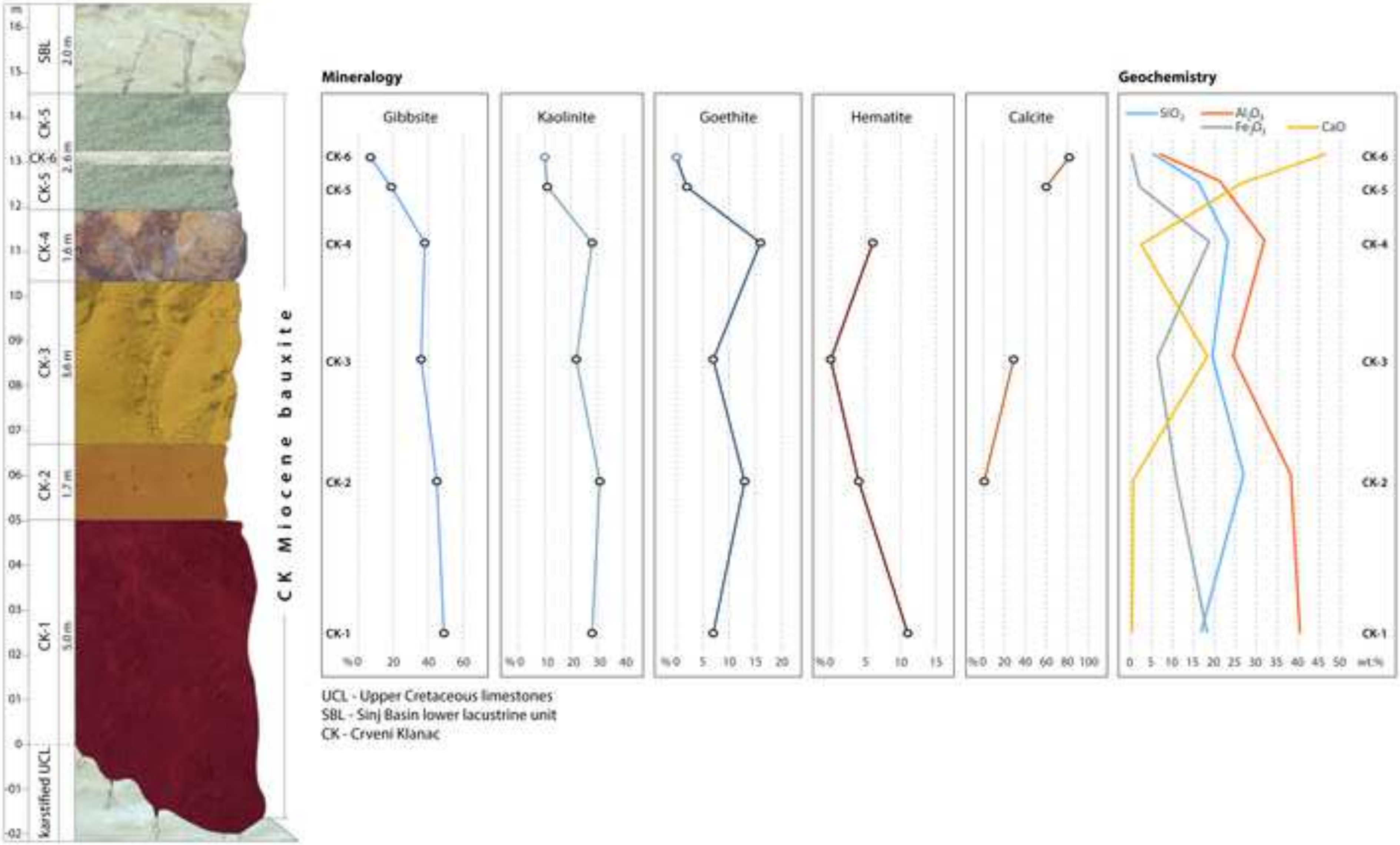
m
16
15
14
13
12
11
10
09
08
07
06
05
04
03
02
01
0
-01
-02
SBL
2.0 m
CK-5
CK-6
CK-5
2.6 m
CK-4
1.6 m
CK-3
3.6 m
CK-2
1.7 m
CK-1
5.0 m
karstified UCL
CK Miocene bauxite
Mineralogy
Gibbsite
Kaolinite
Goethite
Hematite
Calcite
CK-6
CK-5
CK-4
CK-3
CK-2
CK-1
% 0 20 40 60
% 0 10 20 30 40
% 0 5 10 15 20
% 0 5 10 15
% 0 20 40 60 80 100
Geochemistry
SiO₂
Al₂O₃
Fe₂O₃
CaO
0 5 10 15 20 25 30 35 40 45 50 wt.%
UCL - Upper Cretaceous limestones
SBL - Sinj Basin lower lacustrine unit
CK - Crveni Klanac

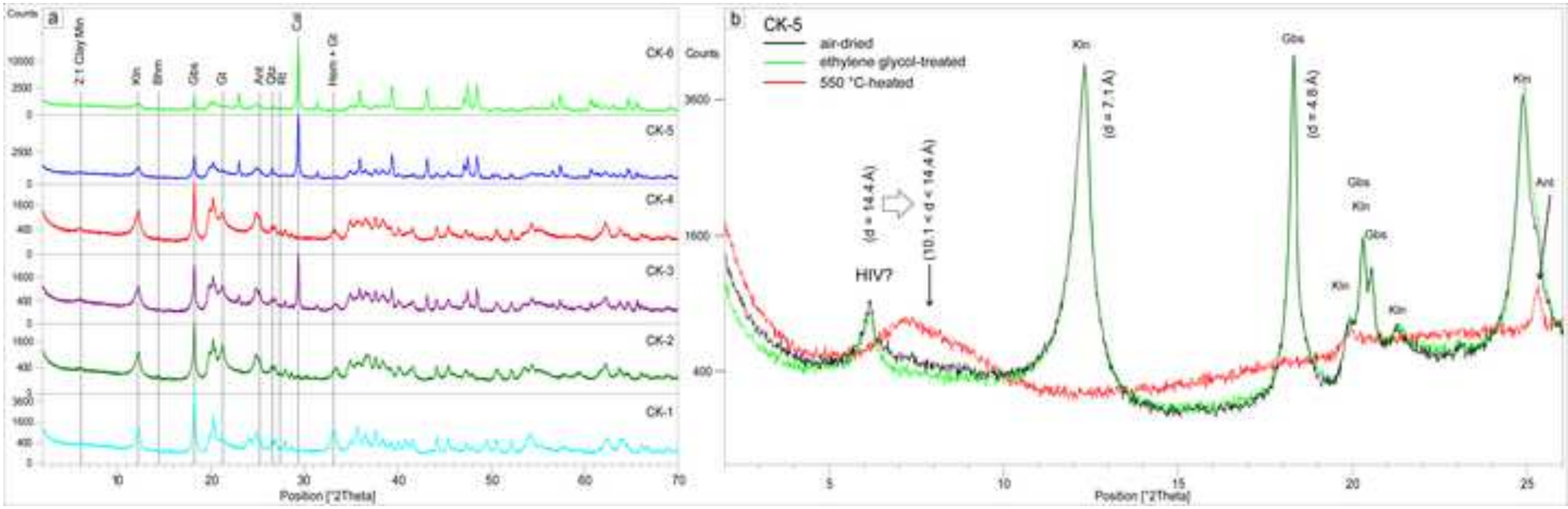
a
Counts
10000
2500
0
2500
0
1600
400
0
1600
400
0
1600
400
0
3600
1600
400
0
2:1 Clay Min
Kln
Bhm
Gbs
Gt
Ant
Qtz
Bt
Cal
Hem + Gt
CK-6
CK-5
CK-4
CK-3
CK-2
CK-1
10
20
30
40
50
60
70
Position [°2Theta]
b
CK-5
air-dried
ethylene glycol-treated
550 °C-heated
Counts
3600
1600
400
Kln
(d = 7.1 Å)
Gbs
(d = 4.8 Å)
(d = 14.4 Å)
(10.1 < d < 14.4 Å)
HIV?
Gbs
Kln
Gbs
Kln
Kln
Kln
Ant
5
10
15
20
25
Position [°2Theta]

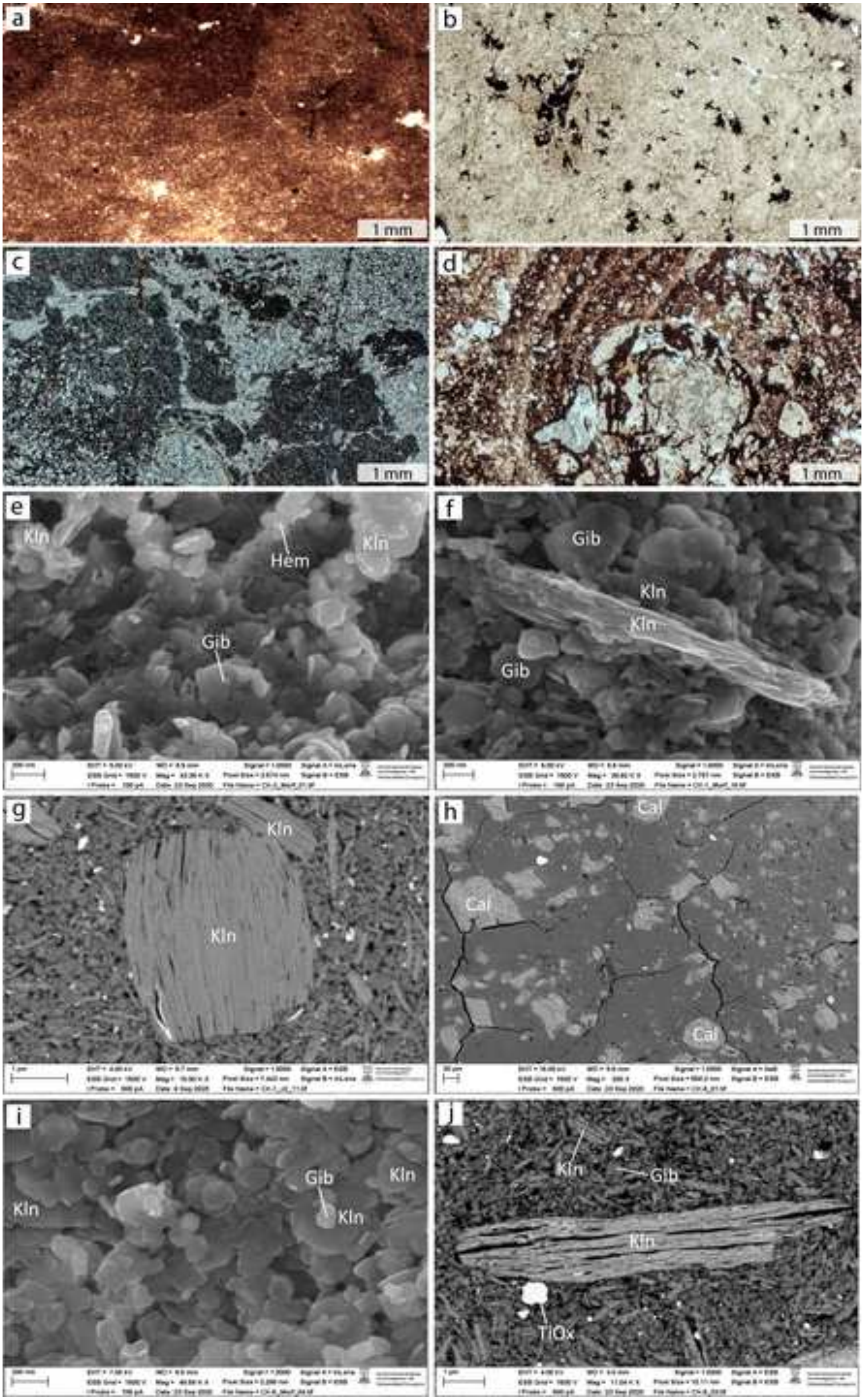
a
1 mm
b
1 mm
c
1 mm
d
1 mm
e
Kln
Hem
Kln
Gib
f
Gib
Kln
Kln
Gib
g
Kln
Kln
h
Cal
Cal
Cal
i
Kln
Gib
Kln
Kln
j
Kln
Gib
Kln
TiOx

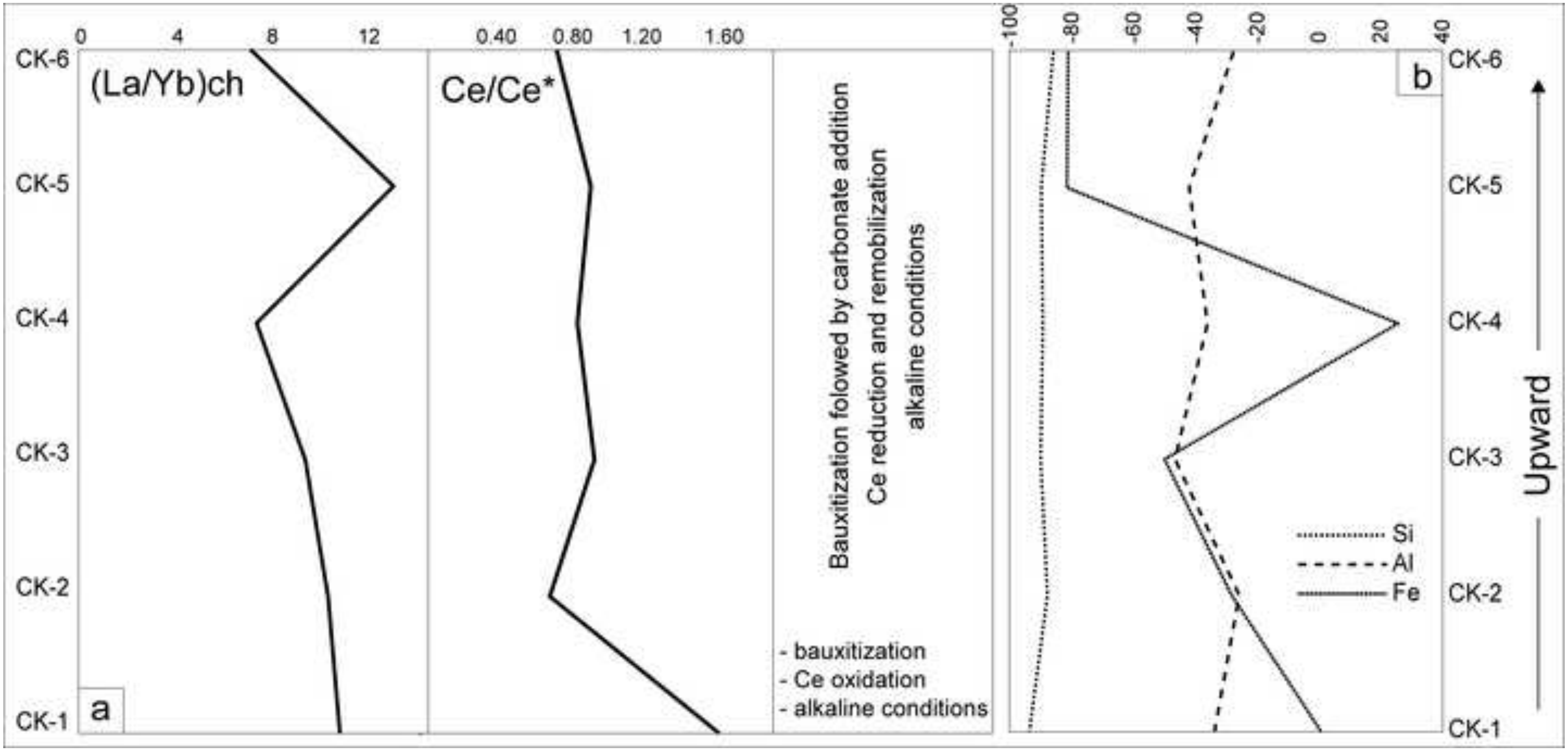
a
(La/Yb)ch
0
4
8
12
Ce/Ce*
0.40
0.80
1.20
1.60
CK-6
CK-5
CK-4
CK-3
CK-2
CK-1
Bauxitization folowed by carbonate addition
Ce reduction and remobilization
alkaline conditions
- bauxitization
- Ce oxidation
- alkaline conditions
b
-100
-80
-60
-40
-20
0
20
40
Si
Al
Fe
Upward

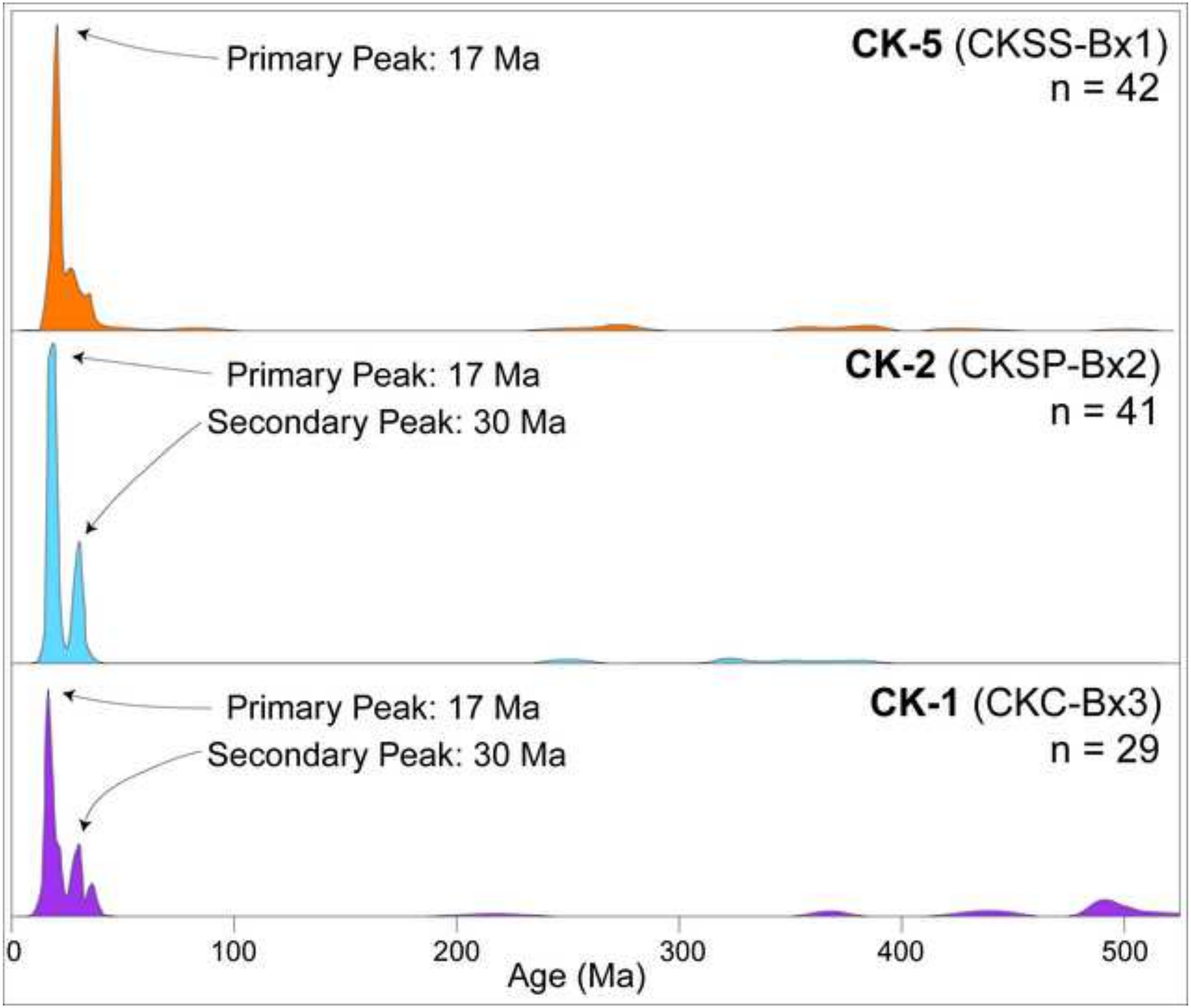
Primary Peak: 17 Ma
CK-5 (CKSS-Bx1)
n = 42
Primary Peak: 17 Ma
Secondary Peak: 30 Ma
CK-2 (CKSP-Bx2)
n = 41
Primary Peak: 17 Ma
Secondary Peak: 30 Ma
CK-1 (CKC-Bx3)
n = 29
0
100
200
300
400
500
Age (Ma)


a CK-5 (CKSS-Bx1)
Z2: 17.566 ± 0.021 Ma
Z7: 18.587 ± 0.073 Ma
Z8: 17.180 ± 0.020 Ma
Z13: 17.130 ± 0.024 Ma
*
Z18: 19.482 ± 0.015 Ma
*
Z19: 208.92 ± 0.28 Ma
Z20: 16.953 ± 0.032 Ma
Z23: 17.123 ± 0.019 Ma
Z27: 86.326 ± 0.040 Ma
Z31: 16.955 ± 0.015 Ma
Z33: 68.483 ± 0.077 Ma
a
b
*
Z36a: 346.22 ± 0.13 Ma
Z36b: 17.415 ± 0.066 Ma
*
Z41: 39.691 ± 0.35 Ma
Z42: 265.29 ± 0.12 Ma
*
Z43: 19.00 ± 0.13 Ma
0 µm
200 µm
b CK-2 (CKSP-Bx2)
b
a
Z1a: 16.96 ± 0.11 Ma
Z1b: 17.214 ± 0.014 Ma
Z4: 17.208 ± 0.014 Ma
Z5: 17.228 ± 0.032 Ma
Z10: 17.062 ± 0.016 Ma
Z11: 18.2709 ± 0.0095 Ma
Z14: 30.353 ± 0.012 Ma
b
a
Z19a: 17.388 ± 0.020 Ma
Z19b: 18.347 ± 0.040 Ma
Z28b: 16.964 ± 0.019 Ma
Z29: 17.057 ± 0.062 Ma
Z33: 18.130 ± 0.020 Ma
Z35: 376.57 ± 0.14 Ma
b
a
Z40a: 17.482 ± 0.022 Ma
Z1b: 17.515 ± 0.024 Ma
Z42: 16.957 ± 0.019 Ma
0 µm
200 µm

Figure

Click here to access/download;Figure;Fig_08.tif

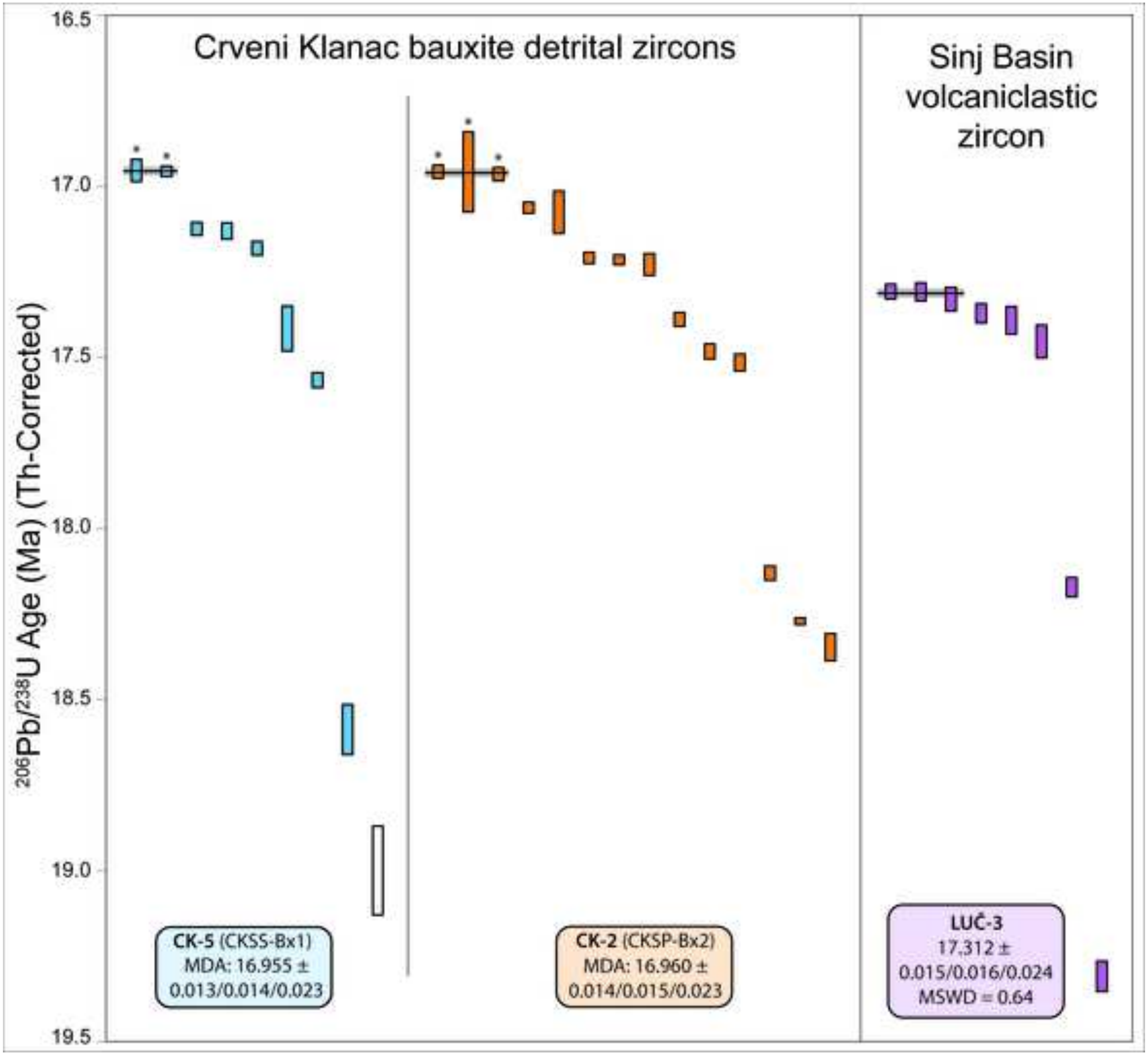

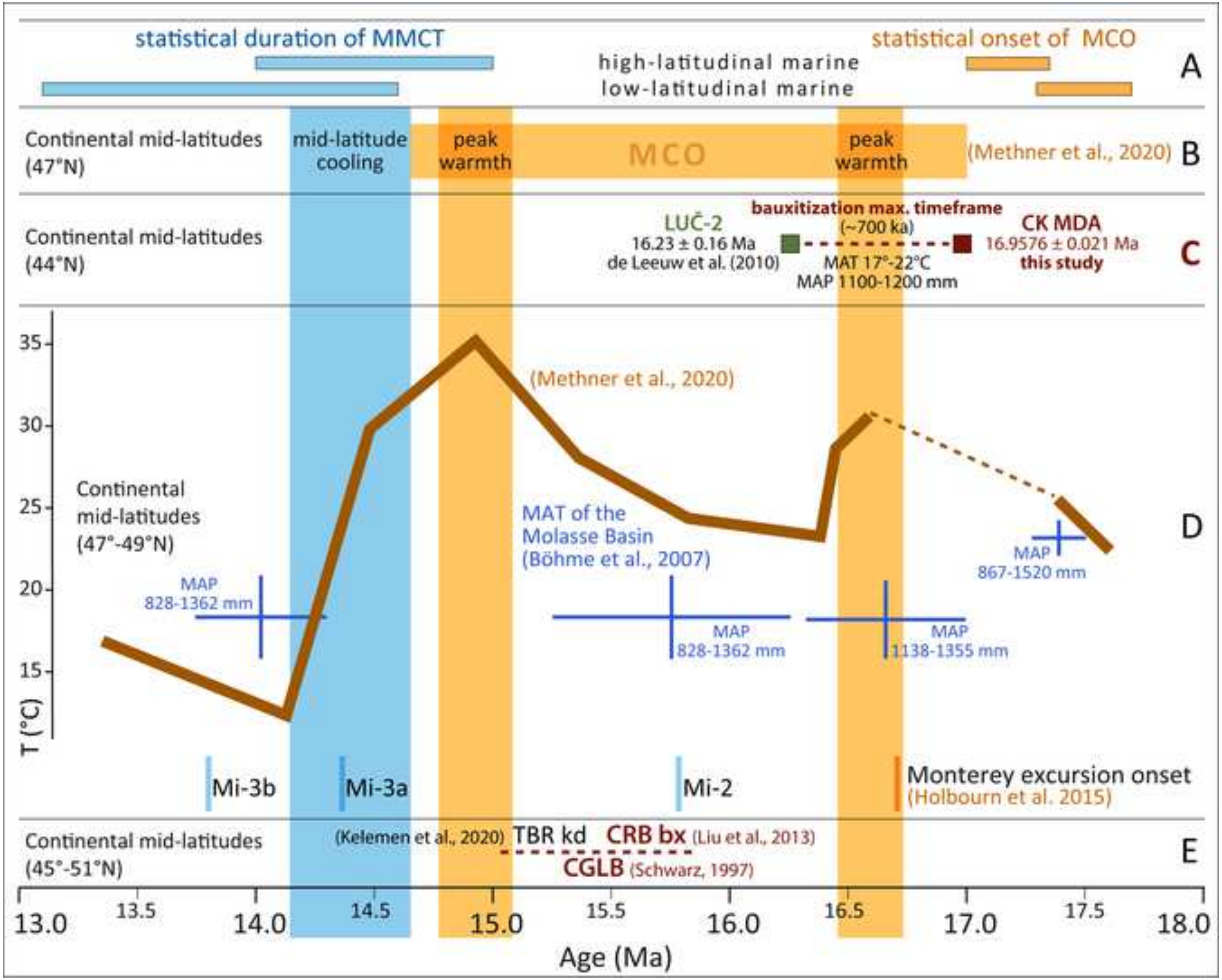
statistical duration of MMCT
statistical onset of MCO
high-latitudinal marine
low-latitudinal marine
A
Continental mid-latitudes (47°N)
mid-latitude cooling
peak warmth
MCO
peak warmth
(Methner et al., 2020)
B
Continental mid-latitudes (44°N)
LUČ-2
16.23 ± 0.16 Ma
de Leeuw et al. (2010)
bauxitization max. timeframe
(~700 ka)
MAT 17°-22°C
MAP 1100-1200 mm
CK MDA
16.9576 ± 0.021 Ma
this study
C
35
30
25
20
15
T (°C)
Continental mid-latitudes (47°-49°N)
(Methner et al., 2020)
MAT of the Molasse Basin (Böhme et al., 2007)
MAP 828-1362 mm
MAP 828-1362 mm
MAP 1138-1355 mm
MAP 867-1520 mm
Mi-3b
Mi-3a
Mi-2
Monterey excursion onset
(Holbourn et al. 2015)
D
Continental mid-latitudes (45°-51°N)
(Kelemen et al., 2020)
TBR kd
CRB bx (Liu et al., 2013)
CGLB (Schwarz, 1997)
E
13.0
13.5
14.0
14.5
15.0
15.5
16.0
16.5
17.0
17.5
18.0
Age (Ma)